PHYSICAL REVIEW D **99,** 063537 (2019)

Constraining power of cosmological observables: Blind redshift spots and optimal ranges

L. Kazantzidis,[*] L. Perivolaropoulos,[†] and F. Skara[‡]
Department of Physics, University of Ioannina, 45110 Ioannina, Greece

(Received 17 December 2018; published 29 March 2019)

A cosmological observable measured in a range of redshifts can be used as a probe of a set of cosmological parameters. Given the cosmological observable and the cosmological parameter, there is an optimum range of redshifts where the observable can constrain the parameter in the most effective manner. For other redshift ranges the observable values may be degenerate with respect to the cosmological parameter values and thus inefficient in constraining the given parameter. These are blind redshift ranges. We determine the optimum and blind redshift ranges of basic cosmological observables with respect to three cosmological parameters: the matter density parameter Ω_m, the equation-of-state parameter w (assumed constant), and a modified gravity parameter g_a which parametrizes a possible evolution of the effective Newton's constant as $G_{\rm eff}(z) = G_N(1 + g_a(1-a)^2 - g_a(1-a)^4)$ (where $a = \frac{1}{1+z}$ is the scale factor and G_N is Newton's constant of general relativity). We consider the following observables: the growth rate of matter density perturbations expressed through $f(z)$ and $f\sigma_8(z)$, the distance modulus $\mu(z)$, baryon acoustic oscillation observables $D_V(z) \times \frac{r_s^{\rm fid}}{r_s}$, $H \times \frac{r_s}{r_s^{\rm fid}}$ and $D_A \times \frac{r_s^{\rm fid}}{r_s}$, $H(z)$ measurements, and the gravitational wave luminosity distance. We introduce a new statistic $S_P^O(z) \equiv \frac{\Delta O}{\Delta P}(z) \cdot V_{\rm eff}^{1/2}$, including the effective survey volume $V_{\rm eff}$, as a measure of the constraining power of a given observable O with respect to a cosmological parameter P as a function of redshift z. We find blind redshift spots z_b ($S_P^O(z_b) \simeq 0$) and optimal redshift spots z_s ($S_P^O(z_s) \simeq \max$) for the above observables with respect to the parameters Ω_m, w, and g_a. For example, for $O = f\sigma_8$ and $P = (\Omega_m, w, g_a)$ we find blind spots at $z_b \simeq (1, 2, 2.7)$, respectively, and optimal (sweet) spots at $z_s = (0.5, 0.8, 1.2)$. Thus, probing higher redshifts may in some cases be less effective than probing lower redshifts with higher accuracy. These results may be helpful in the proper design of upcoming missions aimed at measuring cosmological observables in specific redshift ranges.

DOI: 10.1103/PhysRevD.99.063537

I. INTRODUCTION

The validity of the standard cosmological model (ΛCDM [1]) is currently under intense investigation using a wide range of cosmological observational probes, including cosmic microwave background (CMB) experiments, galaxy photometric and spectroscopic surveys, attempts to measure baryon acoustic oscillations (BAO), weak lensing (WL), redshift-space distortions (RSD), cluster counts, as well as the use of type Ia supernovae (SnIa) as standard candles.

This investigation has revealed the presence of tensions within the ΛCDM model, i.e., inconsistencies among the parameter values determined using different observational probes. The most prominent tension is the H_0 tension which indicates 3σ-level inconsistencies between the value favored by the latest CMB data release from the Planck Collaboration [2,3] [$H_0 = 67.4 \pm 0.5 \,{\rm km s^{-1} Mpc^{-1}}$ (68% confidence limit)] and the local Hubble Space Telescope measurement [4] (based on distance ladder estimates from Cepheids) $H_0 = 73.24 \pm 1.74 \,{\rm km\, s^{-1}\, Mpc^{-1}}$ (68% confidence limit). Another less prominent tension ($2-3\sigma$) is the $\Omega_m - \sigma_8$ tension between the CMB Planck data and the density perturbation growth data (RSD and WL) [5–9]. The CMB data favor higher values of the matter density parameter Ω_m and the matter fluctuations amplitude σ_8 than the data from direct probes of the gravitational interaction (RSD and WL).

A key question therefore arises: are these tensions an early hint of new physics beyond the standard model, or are they a result of systematic/statistical fluctuations in the data?

Completed, ongoing, and future CMB experiments and large-scale structure surveys aim to test the standard ΛCDM model and address the above question. These surveys are classified into four stages. Stages I and II correspond to completed surveys and CMB experiments, while stages III and IV correspond to ongoing and future

---

[*] lkazantzi@cc.uoi.gr
[†] leandros@uoi.gr
[‡] fskara@cc.uoi.gr

projects, respectively. For example, stage II CMB experiments include WMAP [10], Planck [2,3], ACTPol [11], and SPT-Pol [12], while stage III CMB experiments include AdvACT [13] and SPT-3G [14]. Future stage IV CMB probes on the ground [15] and in space such as LiteBIRD [16,17] mainly aim to measure CMB lensing and the CMB-B modes in detail.

A large amount of high-quality data is expected in the coming years from large-scale structure surveys (see Table I). Stage III large-scale structure surveys include the Canada-France-Hawaii Telescope Lensing Survey [18], the Kilo Degree Survey (KiDS) [8,9], the extended Baryon Oscillation Spectroscopic Survey (eBOSS) [19], the Dark Energy Survey (DES) [20–22], and the Hobby-Eberly Telescope Dark Energy Experiment (HETDEX) [23]. Finally, stage IV large-scale structure surveys include ground-based telescopes such as the Dark Energy Spectroscopic Instrument (DESI), the Large Synoptic Survey Telescope (LSST) [24,25], and the Square Kilometer Array [26–29], as well as space-based telescopes such as Euclid [30,31] and the Wide Field Infrared Survey Telescope (WFIRST) [32,33]. The redshift ranges of these and other similar surveys are shown along with their type and duration in Table I. As seen in Table I, the redshift ranges of more recent surveys tend to increase in comparison with earlier surveys. This trend for higher redshifts implies an assumption of increasing constraining power of observables on cosmological parameters with redshift. As demonstrated in the present analysis, however, this assumption is not always true. In this context the following questions arise:

1. What is the redshift dependence of the constraining power of a given observable with respect to a given cosmological parameter?
2. Is there an optimal redshift range where the constraining power of a given observable is maximal with respect to a given cosmological parameter?
3. Are there blind redshift spots where a given observable is degenerate with respect to specific cosmological parameters?

These questions are addressed in the present analysis. Previous studies [34] have indicated the presence of degeneracies for the case of the growth of fluctuations observable $f\sigma_8(z)$ with respect to the equation-of-state parameter w in specific redshift ranges. Here, we extend these results to a wider range of observables and cosmological parameters.

In particular, the goals of the present analysis are the following:

1. Present extensive up-to-date compilations of recent measurements of cosmological observables including the growth of perturbations, BAO, and luminosity distance observables.
2. Identify the sensitivity of these observables as a function of redshift for three cosmological parameters: the present matter density parameter Ω_m, the dark energy equation-of-state parameter w (assumed constant), and a parameter g_a describing the evolution of the effective Newton's constant in the context of a well-motivated parametrization [6,7].
3. Identify possible trends for deviations of the above parameters from their standard Planck15/ΛCDM values in the context of the above data compilations.

The structure of this paper is as follows. In the next section we review the basic equations determining the growth of cosmological density perturbations. These equations can lead to the predicted evolution of the observable product $f(a)\sigma_8(a)$, where a is the scale factor $a = \frac{1}{1+z}$, $f(a) \equiv d\ln\delta(a)/d\ln a$ is the growth rate of cosmological perturbations, $\delta(a) \equiv \delta\rho/\rho$ is the linear matter overdensity growth factor, and σ_8 is the matter power spectrum normalization on scales of $8h^{-1}$ Mpc. In this section we discuss the sensitivity of the observables $f\sigma_8(z)$ and $f(z)$ on the cosmological parameters Ω_m, w, and g_a as a function of redshift. The redshift range of the current available data $f\sigma_8(z)$ that is most constraining on these parameters is also identified and the existence of blind redshift spots where $f\sigma_8(z)$ is insensitive to these parameters is demonstrated. The selection of these particular parameters (Ω_m, w, and g_a)

TABLE I. Some recent and future large-scale structure surveys. Photometric surveys focus mainly on WL, while spectroscopic surveys mainly measure RSD. The redshift ranges shift to higher redshifts for stage III and stage IV surveys.

Survey	z range	Type	Duration	Ref.
SDSS	$0.1 < z < 0.6$	Spectroscopic	2006–2010	[35]
WiggleZ	$0.4 < z < 0.8$	Spectroscopic	2006–2010	[36]
BOSS	0.35, 0.6, 2.5	Spectroscopic	2009–2014	[36]
KIDS	$0 < z < 0.8$	Photometric	2011-	[8,9]
DES	$0.3 < z < 1.0$	Photometric	2012–2018	[20–22]
HETDEX	$1.9 < z < 3.5$	Spectroscopic	2015–2017	[23]
eBOSS	$0.6 < z < 2.2$	Spectroscopic	2015–2018	[19]
DESI	$0.6 < z < 1.7$	Spectroscopic	> 2019	[37–39]
DESI-Bright Galaxies	$0.0 < z < 0.4$	Spectroscopic	> 2019	[37–39]
Euclid	$0.8 < z < 2.0$	Spectroscopic	2022–2027	[30,31,40]
LSST	$0.5 < z < 3$	Photometric	> 2019	[24,25]
WFIRST	$1 < z < 3$	Spectroscopic	> 2020	[32,33]

is important as their combination can lead to direct tests of general relativity (GR) by simultaneously constraining the background expansion rate through $H(z)$ and the possible evolution of the effective Newton's constant. It is important to notice that the evolution of the effective Newton's constant $G_{\rm eff}(z)$ obtained through the parameter g_a is degenerate with $H(z)$ and can only be probed once $H(z)$ is also efficiently constrained through the parameters Ω_m and w.

In Sec. III we focus on cosmological observables obtained from BAO data, present an updated extensive compilation of such data, and identify the sensitivity of the BAO observables on the parameters Ω_m, w, and g_a as a function of redshift. As in the case of the growth observables, blind redshift spots and optimal redshift ranges are identified. The effects of the data redshift range on the shape and size of the uncertainty contours in the above cosmological parameter space are also identified. In Sec. IV we focus on luminosity distance moduli as obtained from type Ia supernovae and gravitational waves and identify the sensitivity of these observables to the parameters Ω_m, w, and g_a as a function of redshift. Binned JLA data are superimposed on the plots to demonstrate the sensitivity of the distance moduli to the cosmological parameters. Finally, in Sec. V we conclude, summarize, and discuss future prospects of the present analysis.

II. GROWTH OF DENSITY PERTURBATIONS: THE OBSERVABLES $f\sigma_8(z)$ AND $f(z)$

The evolution of the linear matter density growth factor $\delta \equiv \delta\rho/\rho$ in the context of both GR and most modified gravity theories on subhorizon scales is described by the equation

$$\ddot{\delta} + 2H\dot{\delta} - 4\pi G_{\rm eff}\rho\delta \approx 0, \tag{2.1}$$

where ρ is the background matter density, $G_{\rm eff}$ is the effective Newton's constant (which in general depends on redshift z and cosmological scale k), and H is the Hubble parameter. In terms of the redshift z, Eq. (2.1) takes the form

$$\delta'' + \left(\frac{(H(z)^2)'}{2H(z)^2} - \frac{1}{1+z}\right)\delta' - \frac{3}{2}\frac{(1+z)\Omega_m G_{\rm eff}(z,k)/G_N}{H(z)^2/H_0^2}\delta = 0, \tag{2.2}$$

while in terms of the scale factor we have

$$\delta''(a) + \left(\frac{3}{a} + \frac{H'(a)}{H(a)}\right)\delta'(a) - \frac{3}{2}\frac{\Omega_m G_{\rm eff}(a,k)/G_N}{a^5 H(a)^2/H_0^2}\delta(a) = 0. \tag{2.3}$$

$G_{\rm eff}$ arises from a generalized Poisson equation,

$$\nabla^2\phi \approx 4\pi G_{\rm eff}\rho\delta, \tag{2.4}$$

where ϕ is the perturbed metric potential in the Newtonian gauge where the perturbed Friedmann-Robertson-Walker metric takes the form

$$ds^2 = -(1+2\phi)dt^2 + a^2(1-2\psi)d\vec{x}^2. \tag{2.5}$$

GR predicts a constant homogeneous $G_{\rm eff}(z,k) = G_N$ (G_N is Newton's constant as measured by local experiments).

Constraints from Solar System [41] and nucleosynthesis tests [42] imply that $G_{\rm eff}$ is close to the GR-predicted form for both low and high redshifts. In particular, at low z we have [41]

$$\left|\frac{1}{G_N}\frac{dG_{\rm eff}(z)}{dz}\right|_{z=0}| < 10^{-3}\ h^{-1}, \tag{2.6}$$

while the second derivative is effectively unconstrained since

$$\left|\frac{1}{G_N}\frac{d^2G_{\rm eff}(z)}{dz^2}\right|_{z=0}| < 10^{5}\ h^{-2}. \tag{2.7}$$

At high z [42] and at 1σ, we have

$$|G_{\rm eff}/G_N - 1| \leq 0.2. \tag{2.8}$$

A parametrization of $G_{\rm eff}(z)$ respecting these constraints is of the form [7]

$$\begin{aligned}\frac{G_{\rm eff}(a,g_a,n)}{G_{\rm N}} &= 1 + g_a(1-a)^n - g_a(1-a)^{n+m} \\ &= 1 + g_a\left(\frac{z}{1+z}\right)^n - g_a\left(\frac{z}{1+z}\right)^{n+m},\end{aligned} \tag{2.9}$$

where n and m are integer parameters with $n \geq 2$ and $m > 0$. Here we set $n = m = 2$.

The observable $f\sigma_8(a)$ can be obtained from the solution $\delta(a)$ of Eq. (2.3) using the definitions $f(a) \equiv d\ln\delta(a)/d\ln a$ and $\sigma(a) = \sigma_8\frac{\delta(a)}{\delta(1)}$. Thus, we have [43]

$$f\sigma_8(a) \equiv f(a)\cdot\sigma(a) \tag{2.10}$$

$$= \frac{\sigma_8}{\delta(1)}a\delta'(a). \tag{2.11}$$

Therefore, both $f\sigma_8(a)$ and the growth rate $f(a)$ [or equivalently $f\sigma_8(z)$ and $f(z)$] can be obtained by numerically solving Eq. (2.2) or Eq. (2.3). The solution of these equations requires the specification of proper parametrizations for both the background expansion $H(z)$ and the effective Newton's constant $G_{\rm eff}(z)$. In the context of the present analysis we assume a flat universe and a wCDM model background expansion of the form

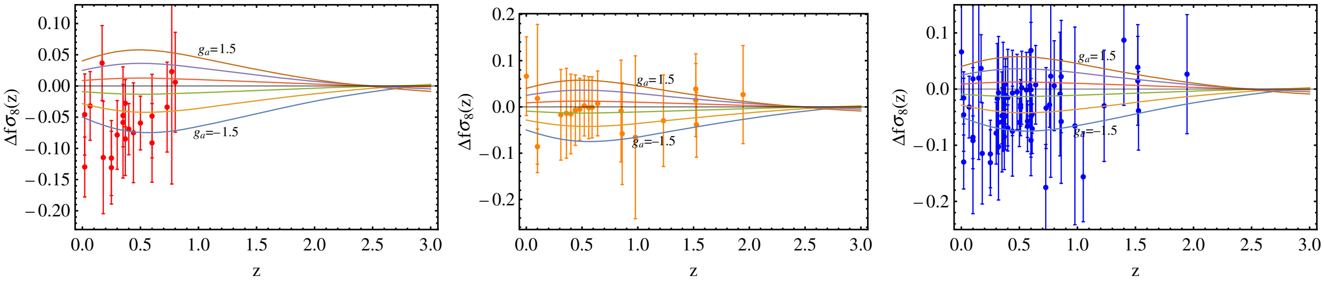

FIG. 1. $\Delta f\sigma_8$ as a function of redshift for various values of g_α superimposed with the early growth data (left panel), late data (middle panel), and full growth data (right panel).

$$H^2(z) = H_0^2[\Omega_m(1+z)^3 + (1-\Omega_m)(1+z)^{3(1+w)}] \Rightarrow$$
$$E^2(z) = \frac{H^2(z)}{H_0^2} = \Omega_m(1+z)^3 + (1-\Omega_m)(1+z)^{3(1+w)}, \tag{2.12}$$

and $G_{\rm eff}$ is parametrized by Eq. (2.9) with $n = m = 2$. Using these parametrizations and initial conditions corresponding to GR in the matter era [$\delta(a) \sim a$], it is straightforward to obtain the predicted evolution of the observables $f\sigma_8(z)$ and $f(z)$ for various parameter values around the standard Planck15/ΛCDM model parameters ($\Omega_m^P = 0.31$, $w = -1$, $g_a = 0$). For each observable $O(\Omega_m, w, g_a)$ [e.g., $f\sigma_8(z)$], we consider the deviation[1]

$$\Delta O_{\Omega_m} \equiv O(\Omega_m, -1, 0) - O(\Omega_m^P, -1, 0). \tag{2.13}$$

Similar deviations ΔO_w and ΔO_{g_a} are defined for the other two parameters in the context of a given observable O.

In Fig. 1 we show the deviation $\Delta f\sigma_{8g_a}$ for g_a in the range $g_a \in [-1.5, 1.5]$ superposed with a recent compilation of the $f\sigma_8(z)$ data [6] shown in Table II in the Appendix (with early data published before 2015 in the left panel, recent data published after 2016 in the middle panel, and the full data set in the right panel). No fiducial model correction has been implemented for the data points shown, but such a correction would lead to a change of no more than about 3% [5,6]. There are three interesting points to be noted in Fig. 1.

1. Early data favor weaker gravity ($g_a < 0$) for redshifts around $z \simeq 0.5$ assuming a fixed Planck15/ΛCDM background. This trend is well known [5] and has been demonstrated and discussed extensively, e.g., in Refs. [7,44–51].
2. The observable $f\sigma_8(z)$ has a blind spot with respect to the parameter g_a at redshift $z \simeq 2.7$. Such a blind spot was also pointed out in Ref. [34] with respect to a similar gravitational strength parameter (where it was called the "sweet spot," even though the term "blind spot" should have been used).
3. There is a redshift range around $z \simeq 0.5$ of optimal sensitivity of the observable $f\sigma_8(z)$ with respect to the parameter g_a. Despite the existence of this optimal redshift range, much of the recent $f\sigma_8(z)$ data appear at larger redshifts approaching the blind spot region. These data points have reduced sensitivity in identifying deviations of $G_{\rm eff}$ from its GR value G_N.

The existence of blind spots and optimal redshifts of an observable O with respect to a cosmological parameter P may also be quantified by defining the "sensitivity" measure including the effects of the survey volume $V_{\rm eff}(k,z)$. The effective survey volume probed for a particular k mode with the power spectrum $p(k,z)$ in a survey of sky area $\Delta\Omega$ is given by

$$V_{\rm eff}(k,z) = \Delta\Omega \int_0^z \left[\frac{n(z')p(k,z')}{1+n(z')p(k,z')}\right]^2 \frac{dV}{dz'd\Omega} dz', \tag{2.14}$$

where z is the maximum redshift corresponding to the survey volume $V_{\rm eff}$ and $n(z)$ is the number density of galaxies that are detected, which is given as

$$n(z) = \int_{M_{\rm lim}(z)}^{\infty} \frac{dN}{dVdM} dM. \tag{2.15}$$

The function $M_{\rm lim}(z)$ is the limiting mass threshold which is detected for the given survey and dV is the infinitesimal comoving volume element,

$$dV = \frac{r^2(z)}{H(z)} d\Omega dz, \tag{2.16}$$

where

$$r(z) = \frac{c}{H_0} \int_0^z \frac{dz'}{E(z')}, \tag{2.17}$$

and $E(z')$ is given by Eq. (2.12).

The constraining power of the observable O depends on the survey volume $V_{\rm eff}(k,z)$, since the error σ_p on the

---

[1] In certain cases we consider the deviation around $\Omega_m = 0.3$ instead of $\Omega_m = \Omega_m^P$.

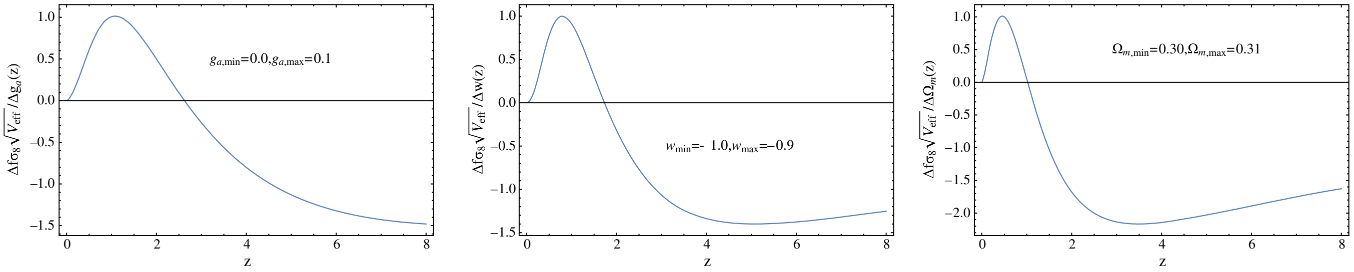

FIG. 2. The sensitivity measure of $\frac{\Delta f\sigma_8}{\Delta P}V_{\rm eff}^{1/2}$ for $P = g_a$ (left panel), $P = w$ (middle panel), and $P = \Omega_m$ (right panel).

measurement of the power spectrum $p(k,z)$ increases as the effective survey volume $V_{\rm eff}(k,z)$ decreases (i.e., as less k modes are measured by the survey) as [90–93]

$$\left(\frac{\sigma_p}{p(k,z)}\right)^2 = \frac{2}{4\pi k^3\Delta(logk)}\frac{(2\pi)^3}{V_{\rm eff}(k,z)}\left[\frac{1+n(z)p(k,z)}{n(z)p(k,z)}\right]^2. \tag{2.18}$$

Thus, since the error σ_p on the measurement of the power spectrum $p(k,z)$ is inversely proportional to the square root of the survey volume $V_{\rm eff}(k,z)$ [see Eq. (2.18)], we define the "sensitivity" measure as

$$S_P^O \equiv \frac{\Delta O(P)}{\Delta P}\cdot V_{\rm eff}(k,z)^{1/2}, \tag{2.19}$$

where ΔO is the deviation of the observable O when a given parameter varies in a fixed small range $\Delta P = P_{\max} - P_{\min}$ around a fiducial model value (e.g., Planck15/ΛCDM). In Fig. 2 we show a plot of the sensitivity measure S for the observable $f\sigma_8(z)$ and the three parameters Ω_m, w, and g_a. The existence of blind spots is manifest as roots of the sensitivity measure, while optimal redshifts appear as maxima of the magnitude of S. We have fixed k such that $np = 3$ assuming sufficient signal to noise per pixel [92]. We have also rescaled the sensitivity measure statistic so that it is unity at its maximum absolute value. The nonlinear modes may be excluded by setting a minimum redshift which is of $O(10^{-2})$ and are much smaller than the derived optimal redshifts and blind spots identified in our analysis. Notice that the sensitivity measure indicates the presence of blind spots for all three parameters. For w the blind spot is close to $z \simeq 2$, while for Ω_m it is close to $z \simeq 1$. The corresponding optimal redshifts are at $z \simeq 1.2$ for g_a, $z \simeq 0.8$ for w, and $z \simeq 0.5$ for Ω_m. (Although the region $z > 2$ for w and Ω_m provides better sensitivity, there is currently almost no data available in this redshift range.) Notice also in Figs. 1 and 2 that when including the effects of the survey volume the optimal redshifts shift to somewhat higher redshifts, while the blind spots remain unaffected.

As shown in Figs. 3 and 4 for both cases, recent data approach the blind spot regions in contrast to early published data that efficiently probed the optimal redshift regions for both parameters w and Ω_m. Also, early data seem to favor weaker growth of perturbations, which occurs for lower g_a and Ω_m and higher w [5–7]. If this trend is partly attributed to a lower value of $G_{\rm eff}$ in the recent past, then it is difficult to reconcile with the most generic modified gravity theories like $f(R)$ and scalar-tensor theories [7,94].

A similar analysis can be performed for the growth rate observable $f(z)$ which will be probed by the Euclid mission [31]. Mock Euclid data assuming a Planck15/ΛCDM fiducial model are shown in Fig. 5 with proper redshifts and error bars [31], along with the deviation of the observable $f(z)$ with respect to Ω_m (left panel), w (middle panel), and g_a (right panel). Clearly, the predicted redshift range of the Euclid data is optimal for the identification of new gravitational physics (right panel), but it is not optimized for constraining the matter density parameter (left panel of Fig. 5) or the equation-of-state parameter if $w < -1$ (middle panel).

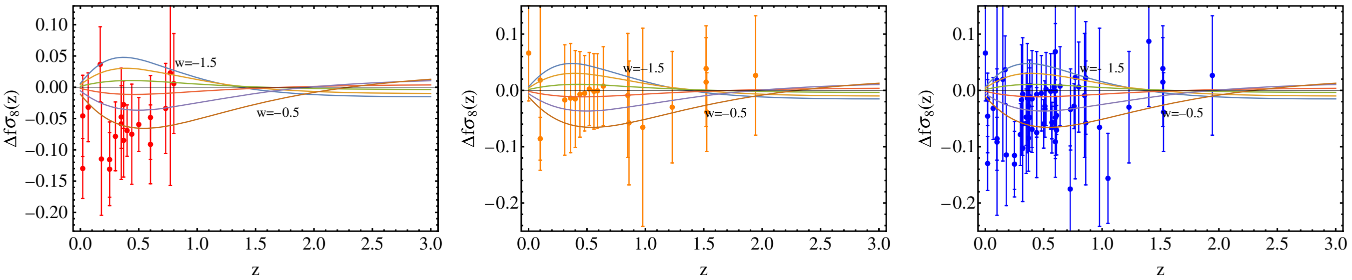

FIG. 3. Same as Fig. 1 for various values of w.

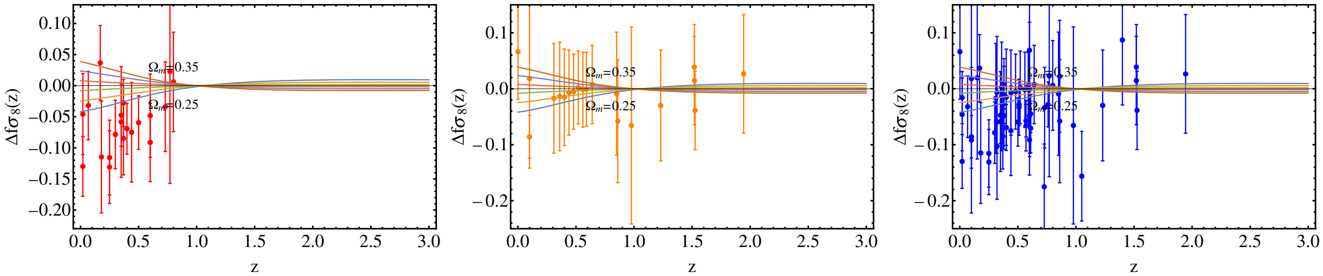

FIG. 4. Same as Fig. 1 for various values of Ω_m.

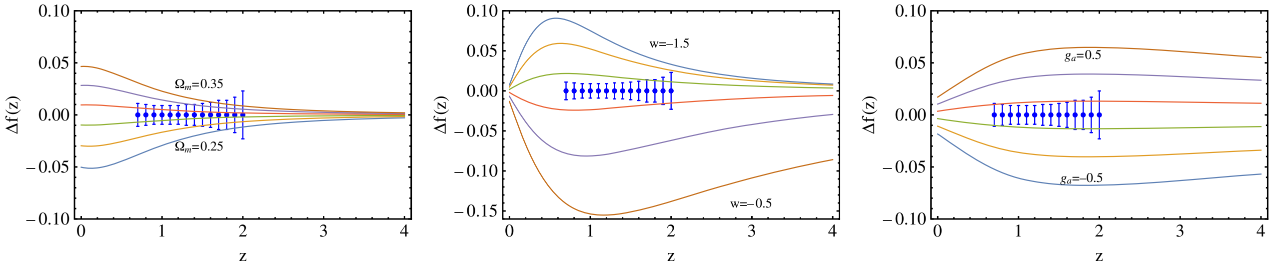

FIG. 5. $\Delta f(z)$ as a function of redshift superimposed with the Euclid mock data for different values of Ω_m (left panel), w (middle panel), and g_α (right panel).

The observable $f(z)$ is considered due to the approach of Ref. [31], where the Euclid team indicated that the large number of galaxies of the Euclid survey combined with the depth of the survey will allow a reliable estimate of the bias simultaneously with the growth rate $f(z)$ obtained through the redshift distortion β. The redshift distortion β is defined as

$$\beta(z) = \frac{\Omega_m(z)^\gamma}{b(z)} = \frac{f(z)}{b(z)}, \tag{2.20}$$

where $b(z)$ is the bias. Thus, the survey will not only probe the bias-free combination $f\sigma_8$, but also directly probe the growth observable $f(z)$, which was modeled in Ref. [31] with error bars and is also considered separately in our analysis. Of course, what is actually observable is the redshift distortion $\beta(z)$ which is obtained through the ratio between the monopoles of the correlation functions in real and redshift space. Thus, the derived blind spot and optimal redshift for the growth rate $f(z)$ are accurate under the assumption that the bias $b(z)$ has a very weak dependence on the redshift.

III. BARYON ACOUSTIC OSCILLATIONS: THE OBSERVABLES $D_V(z) \times \frac{r_s^{\rm fid}}{r_s}$, $H \times \frac{r_s}{r_s^{\rm fid}}$, AND $D_A \times \frac{r_s^{\rm fid}}{r_s}$

A. BAO observables and their variation with cosmological parameters

Waves induced by radiation pressure in the prerecombination plasma inflict a characteristic BAO scale on the late-time matter clustering at the radius of the sound horizon, defined as

$$r_s = \int_{z_d}^{\infty} \frac{c_s(z)}{H(z)} dz, \tag{3.1}$$

where c_s is given by [95]

$$c_s(z) = \frac{c}{\sqrt{3(1 + \frac{3\Omega_b}{4\Omega_\gamma}\frac{1}{1+z})}} \tag{3.2}$$

and the drag redshift z_d corresponds to times shortly after recombination, when photons decouple from baryons [96]. This BAO scale appears as a peak in the correlation function or equivalently as damped oscillations in the large-scale structure power spectrum. In the context of standard matter and radiation epochs, the Planck 2015 measurements of the matter and baryon densities Ω_m and Ω_b specify the BAO scale to great accuracy (uncertainty less than 1%). An anisotropic BAO analysis measuring the sound horizon scale along the line of sight and along the transverse direction can measure both $H(z)$ and the comoving angular diameter distance $D_M(z)$ related to the physical angular diameter distance in a flat universe,

$$D_A(z) = \frac{1}{1+z}\int_0^z \frac{cdz}{H(z)}, \tag{3.3}$$

as $D_M(z) = (1+z)D_A(z)$ [97]. Deviations of cosmological parameters can change r_s, so BAO measurements actually constrain the combinations $D_M(z) \times \frac{r_s^{\rm fid}}{r_s}$, or equivalently $D_A(z) \times \frac{r_s^{\rm fid}}{r_s}$, $H(z) \times \frac{r_s}{r_s^{\rm fid}}$, where $r_s^{\rm fid}$ is the sound horizon (BAO scale) in the context of the fiducial

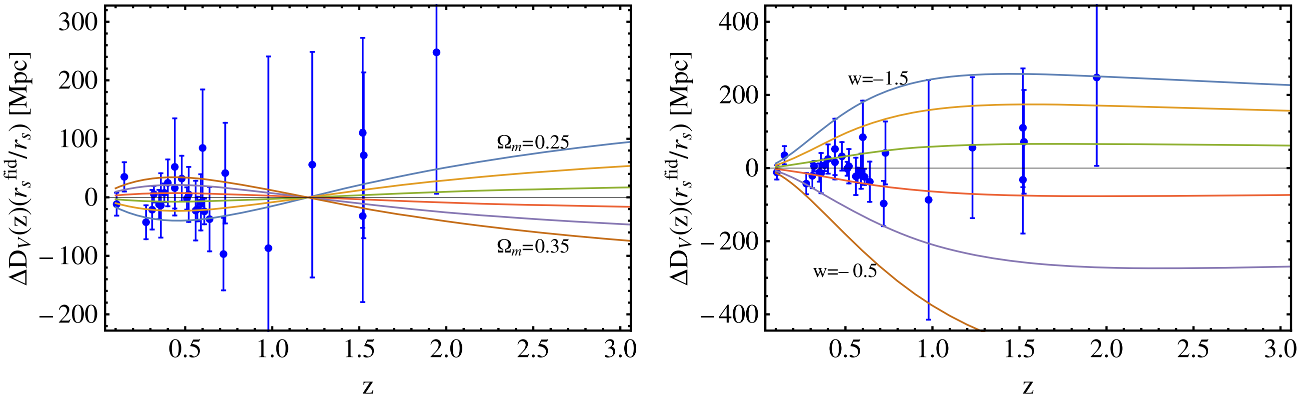

FIG. 6. The deviation $\Delta D_V(z) \times \frac{r_s^{\rm fid}}{r_s}$ as a function of redshift z for different values of Ω_m (left panel) and w (right panel).

cosmology assumed in the construction of the large-scale structure correlation function. An angle-averaged galaxy BAO measurement constrains the combination

$$D_V(z) = [czD_M(z)^2/H(z)]^{1/3}. \tag{3.4}$$

Taking into account the variation of cosmological parameters the constrained combination becomes $D_V(z) \times \frac{r_s^{\rm fid}}{r_s}$. Statistical isotropy can be used to constrain the observable combination $H(z)D_M(z)$ using an anisotropic BAO analysis in the context of the Alcock-Paczynski test [98]. The sound horizon $r_s(z_d)$ at the drag epoch z_d that enters the BAO observables may be calculated in the context of a given cosmological model, either numerically (e.g., with CAMB [99]) or using a fitting formula for z_d [100] of the form

$$z_d = \frac{1291(\Omega_m h^2)^{0.251}}{1 + 0.659(\Omega_m h^2)^{0.828}}[1 + b_1(\Omega_b h^2)^{b_2}], \tag{3.5}$$

where

$$b_1 = 0.313(\Omega_m h^2)^{-0.419}[1 + 0.607(\Omega_m h^2)^{0.674}], \tag{3.6}$$

$$b_2 = 0.238(\Omega_m h^2)^{0.223}, \tag{3.7}$$

and from Eq. (3.1)

$$r_s(z) = \frac{c}{\sqrt{3}}\int_{z_d}^{\infty} \frac{dz}{H(z)\sqrt{1 + \frac{3\Omega_b}{4\Omega_\gamma}\frac{1}{1+z}}}, \tag{3.8}$$

where $\Omega_\gamma = 2.469 \times 10^{-5} h^{-2}$ for $T_{\rm cmb} = 2.725$ K, and

$$H(z) = H_0[\Omega_m(1+z)^3 + \Omega_r(1+z)^4 + \Omega_\Lambda(1+z)^{3(1+w)}]^{1/2}, \tag{3.9}$$

with $\Omega_r = \Omega_\gamma(1 + 0.2271 N_{\rm eff})$ ($N_{\rm eff} \simeq 3$ is the number of neutrino species) and

$$\Omega_m + \Omega_r + \Omega_\Lambda = 1 \tag{3.10}$$

in the context of a flat universe. It has been shown [101] that when the fitting formula is used to obtain z_d close to the Planck15/ΛCDM parameter values, a correction factor of 154.66/150.82 should be used on r_s obtained from Eq. (3.8) to obtain agreement with the more accurate numerical estimate of r_s. Using Eqs. (3.3), (3.4), and (3.8) and a Planck15/ΛCDM fiducial cosmology ($h = 0.676$, $\Omega_b h^2 = 0.0223$, $\Omega_m = 0.31$, and $r_s^{\rm fid} = 147.49$ Mpc), it is straightforward to construct the theoretically predicted redshift dependence of the BAO observables $D_V(z) \times \frac{r_s^{\rm fid}}{r_s}$, $H \times \frac{r_s}{r_s^{\rm fid}}$, and $D_A \times \frac{r_s^{\rm fid}}{r_s}$ for various values of the parameters Ω_m and w and superpose this dependence with the corresponding currently available data shown in Table III in the Appendix.

In Fig. 6 we show the predicted evolution of the deviation of the observable $D_V(z) \times \frac{r_s^{\rm fid}}{r_s}$ for various values of Ω_m (left panel) and w (right panel). The deviation of the parameter Ω_m (left panel) was performed around the value $\Omega_m = 0.3$, while the deviation of the parameter w was performed around the ΛCDM value $w = -1$ [see Eq. (2.13)]. Notice the existence of a blind spot at $z \simeq 1.2$ for the observable $D_V(z) \times \frac{r_s^{\rm fid}}{r_s}$ with respect to the parameter Ω_m, while the optimal redshift in the same plot is $z \simeq 0.6$. (Even though the region $z > 2$ also seems to be optimal, there is currently almost no data available in this redshift range.) In contrast, for the same observable with respect to the parameter w there is no blind spot, while the optimal redshift range is $z > 1.2$.

In Fig. 7 we show the predicted evolution of the deviation of the observable $H \times \frac{r_s}{r_s^{\rm fid}}$ for various values of Ω_m (left panel) and w (right panel). For this observable there is no blind redshift spot, while the sensitivity appears to increase monotonically with redshift for both observables. Notice the asymmetry obtained for the equation-of-state parameter which is due to the fact that for $w < -1$ at early times the effects of dark energy are negligible for all

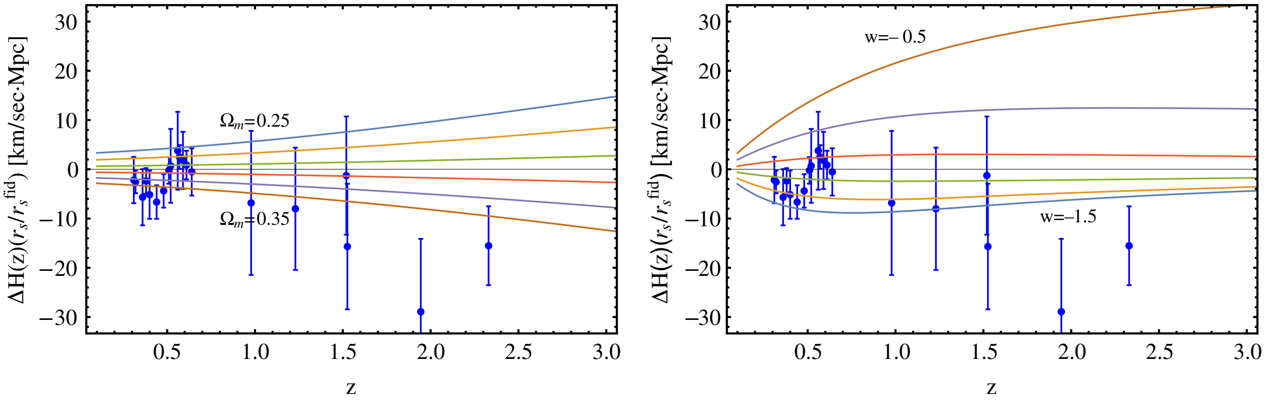

FIG. 7. The deviation $\Delta H \times \frac{r_s}{r_s^{\rm fid}}$ as a function of redshift z for different values of Ω_m (left panel) and w (right panel).

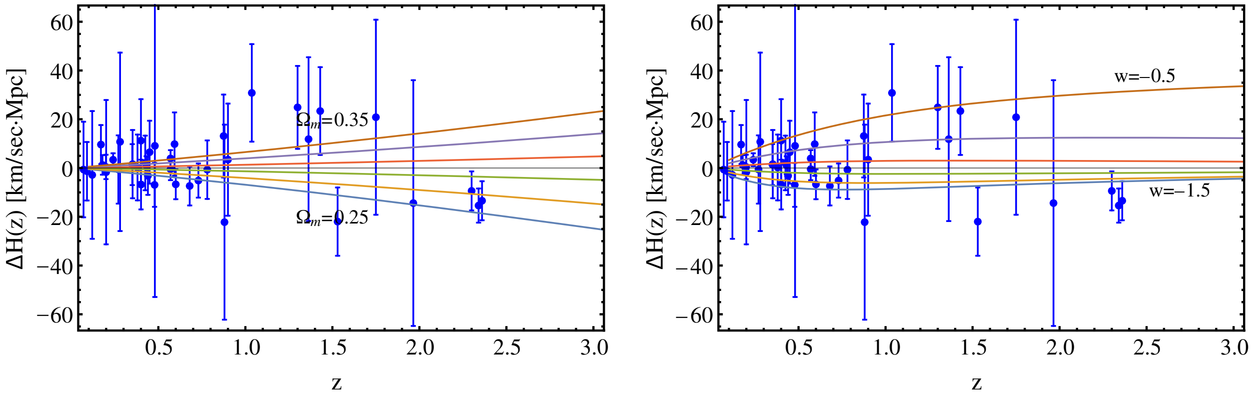

FIG. 8. The deviation $\Delta H(z)$ as a function of redshift using the full compilation of Table IV in the Appendix, for various values of Ω_m (left panel) and w (right panel).

values of w, leading to a degeneracy for this range of parameters at high z. For comparison, in Fig. 8 we show the deviation of the observable Hubble expansion rate for various values of Ω_m (left panel) and w (right panel) along with the corresponding data obtained from the spectroscopic evolution of galaxies used as cosmic chronometers, as shown in Table IV in the Appendix with the corresponding citations (for previous compilations, see also Refs. [102–104]). Even though Figs. 7 and 8 are qualitatively similar, it is clear that the BAO data are significantly more constraining compared to the cosmic chronometer data with respect to both parameters Ω_m and w, especially at low redshifts.

In Fig. 9 we show the predicted evolution of the deviation of the observable $D_A \times \frac{r_s^{\rm fid}}{r_s}$ for various values of Ω_m (left panel) and w (right panel). The behavior of this observable is similar to that of $D_V(z) \times \frac{r_s^{\rm fid}}{r_s}$ even though the

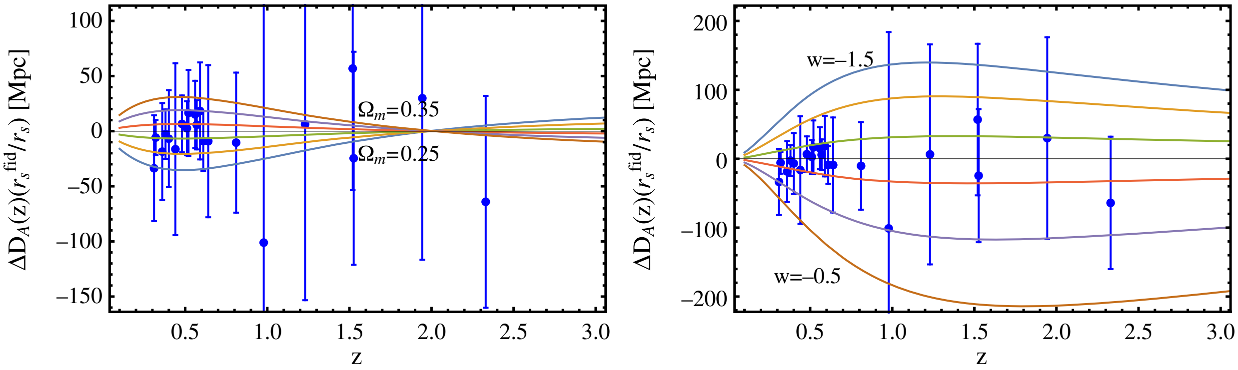

FIG. 9. The deviation $\Delta D_A \times \frac{r_s^{\rm fid}}{r_s}$ as a function of redshift z for different values of Ω_m (left panel) and w (right panel).

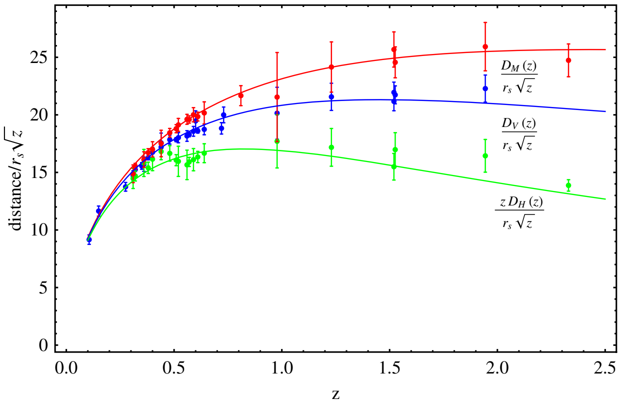

FIG. 10. The BAO observable distances for the Planck15/ΛCDM best-fit parameter values along with the corresponding data from Table III in the Appendix. The data appear to be in good agreement with the Planck15/ΛCDM predictions.

blind spot with respect to the parameter Ω_m appears at a higher redshift ($z \simeq 2$), while at higher redshifts the sensitivity of this observable with respect to the parameter Ω_m is significantly reduced compared to the sensitivity of $D_V(z) \times \frac{r_s^{\rm fid}}{r_s}$.

A comparison of the three BAO observable distances $\frac{D_M(z)}{r_s\sqrt{z}}$, $\frac{D_V(z)}{r_s\sqrt{z}}$, and $\frac{zD_H(z)}{r_s\sqrt{z}}$ [as $D_H(z) = \frac{c}{H(z)}$] for the Planck15/ΛCDM best-fit parameter values along with the corresponding data from Table III in the Appendix is shown in Fig. 10. This plot is in excellent agreement with the corresponding plot of Ref. [73] (Fig. 14) even though here we superpose the Planck15/ΛCDM prediction with a significantly larger compilation of data points. As demonstrated in the next subsection, the BAO data are in good agreement with the Planck15/ΛCDM parameter values.

B. Contour shapes and redshift ranges

The existence of optimal and blind redshift ranges for the BAO observables with respect to cosmological parameters has an effect on the form of maximum likelihood contours obtained from data at various redshift ranges. In particular, the figure of merit (the reciprocal of the area of confidence contours in parameter space) tends to decrease for data sets with redshifts close to blind redshift spots and increase for data sets with redshifts close to optimal redshift regions. In order to demonstrate this effect, we construct the confidence contours for the parameters Ω_m and w using the BAO observables in different redshift regions.

In order to construct χ^2 we first consider the vector

$$V^i_{\rm BAO}(z_i, \Omega_m, w) \equiv {\rm BAO}^m_i - {\rm BAO}^m_{\rm theoretical}, \tag{3.11}$$

where m runs from 1 to 3, indicating the different types of BAO data in Table III in the Appendix, and the theoretical expressions for $D_A \times \frac{r_s^{\rm fid}}{r_s}$, $D_V(z) \times \frac{r_s^{\rm fid}}{r_s}$ and $H \times \frac{r_s}{r_s^{\rm fid}}$ are given in Eqs. (3.3), (3.4), and (3.9), respectively. χ^2 is obtained as

$$\chi^2 = V^i F_{ij} V^j, \tag{3.12}$$

where F_{ij} is the Fisher matrix (inverse of the covariance matrix C_{ij}).

The covariance matrix for the $D_V(z) \times \frac{r_s^{\rm fid}}{r_s}$ data takes the form

$$C^{\rm BAO,total}_{ij,D_V\times(r_s^{\rm fid}/r_s)} = \begin{pmatrix} \sigma_1^2 & 0 & 0 & \cdots \\ 0 & C^{\rm WiggleZ}_{ij} & 0 & \cdots \\ 0 & 0 & \cdots & \sigma_N^2 \end{pmatrix}, \tag{3.13}$$

where $N = 28$ and [105]

$$C^{\rm WiggleZ}_{ij} = F^{-1}_{ij,{\rm WiggleZ}} = 10^4 \begin{pmatrix} 2.18 & -1.12 & 0.47 \\ -1.12 & 1.71 & -0.72 \\ 0.47 & -0.72 & 1.65 \end{pmatrix}^{-1}, \tag{3.14}$$

whereas for both $D_A \times \frac{r_s^{\rm fid}}{r_s}$ and $H \times \frac{r_s}{r_s^{\rm fid}}$ we have assumed a diagonal covariance matrix

$$C^{\rm BAO,total}_{ij} = \begin{pmatrix} \sigma_1^2 & 0 & 0 & \cdots \\ 0 & \sigma_2^2 & 0 & \cdots \\ 0 & 0 & \cdots & \sigma_N^2 \end{pmatrix}, \tag{3.15}$$

where N is equal to the considered number of data points.

The forms of Eqs. (3.13) and (3.15) are clearly oversimplifications of the actual covariance matrices, since these forms ignore possible correlations between the considered BAO data. However, to the best of our knowledge the nondiagonal terms of the D_A and H covariance matrices are not publicly available. In order to estimate the magnitude of the effects of these terms we have performed Monte Carlo simulations including random nondiagonal terms to the covariance matrices for D_A and H of relative magnitude similar to the nondiagonal terms of the nondiagonal terms corresponding to D_V setting the magnitude of the matrix [6]

$$C_{ij} = \frac{1}{2}\sigma_i \cdot \sigma_j, \tag{3.16}$$

where σ_i and σ_j are the errors of the published data points i and j, respectively. These simulations indicated that the likelihood contours and the best-fit parameter values do not change more than 10% when we include the nondiagonal terms in the covariance matrix. Thus, possible reasonable correlations among data points are not expected to significantly affect our results [106].

In the left panel of Fig. 11 we show the 1σ–3σ Ω_m-w contour plots for the full $D_V(z) \times \frac{r_s^{\rm fid}}{r_s}$ data of Table III in the

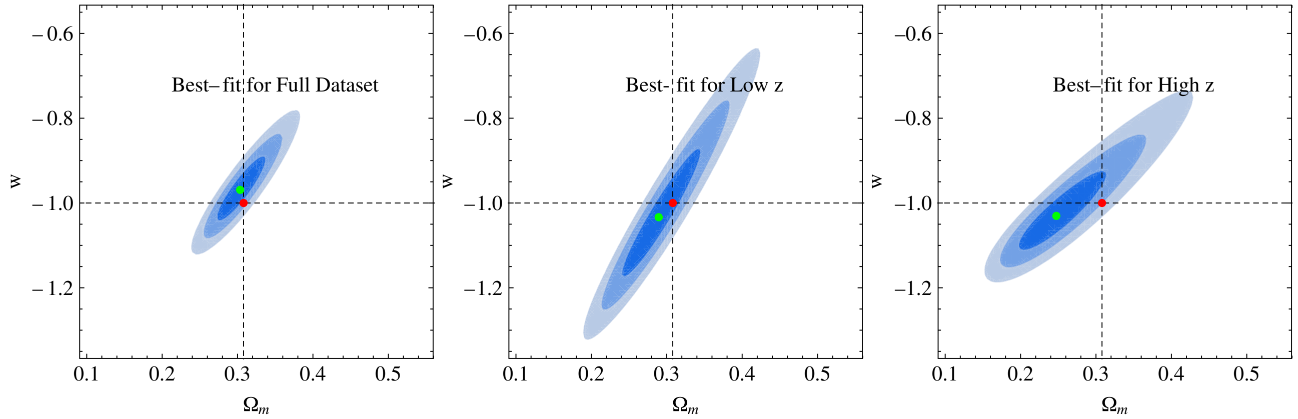

FIG. 11. The 1σ–3σ contours in Ω_m-w parametric space. The contours describe the corresponding confidence regions using the full compilation of $D_V(z)\times\frac{r_s^{\rm fid}}{r_s}$ data (left panel), low redshift ($z<0.55$) data (middle panel), and high redshift ($z>0.55$) data (right panel) from Table III in the Appendix. The red and green dots describe the Planck15/ΛCDM best fit and the best-fit values from the compilation of $D_V(z)\times\frac{r_s^{\rm fid}}{r_s}$ data. Notice that at high z close to the blind spot for Ω_m and the optimum redshift for w, the thickness of the contours (uncertainty) increases along the Ω_m axis and decreases along the w axis (the contours are rotated clockwise), as expected from Fig. 6.

Appendix using Eqs. (3.11)–(3.13) and ignoring the possible correlations among the data points. The best-fit parameter values are within 1σ from the corresponding best-fit Planck15/ΛCDM values (red dot).

Furthermore, we construct the same contour plots for low-redshift $D_V(z)\times\frac{r_s^{\rm fid}}{r_s}$ data (middle panel of Fig. 11), where $z<0.55$ (14 data points), and for high-redshift $D_V(z)\times\frac{r_s^{\rm fid}}{r_s}$ data (right panel of Fig. 11), where $z>0.55$ (14 data points). The low-redshift data correspond to optimal redshift for the parameter Ω_m (see Fig. 6) and thus the confidence contours are thinner in the direction of the Ω_m axis, while the contours are elongated in the w direction. In contrast, the high-redshift data are close to the Ω_m blind spot and thus the confidence contours are thicker in the Ω_m direction (left panel), while the contours are suppressed in the w direction (as expected from Fig. 6) which indicates an optimal high-redshift range for the parameter w.

Similar conclusions and confidence contours are obtained from the low- and high-redshift data for $D_A\times\frac{r_s^{\rm fid}}{r_s}$ and $H\times\frac{r_s}{r_s^{\rm fid}}$ data (see Supplemental Material [106]).

IV. DISTANCE MODULI FROM SnIa AND GRAVITATIONAL WAVES

The luminosity distance

$$D_L(z;\Omega_m,w)=(1+z)\int_0^z\frac{cdz}{H(z;\Omega_m,w)}\qquad(4.1)$$

is an important cosmological observable that is measured using standard candles like SnIa or standard gravitational wave sirens, like merging binary neutron star systems observed via multimessenger observations. The distance modulus $\mu=m-M$ is the difference between the apparent magnitude m and the absolute magnitude M of standard candle. It is related to the luminosity distance D_L in Mpc as

$$\mu(z;\Omega_m,w)=5\log_{10}(D_L)+25.\qquad(4.2)$$

In the context of a varying effective Newton's constant $G_{\rm eff}(z)$ the absolute magnitude of SnIa is expected to vary with redshift as [107–109]

$$M-M_0=\frac{15}{4}\log_{10}\left(\frac{G_{\rm eff}}{G_N}\right),\qquad(4.3)$$

where the subscript 0 refers to the local value of M. Thus, for SnIa μ also depends on the evolution of $G_{\rm eff}(z)$ (or equivalently on the parameter g_a) as

$$\mu(z;\Omega_m,w,g_a)=5\log_{10}(D_L)+\frac{15}{4}\log_{10}\left(\frac{G_{\rm eff}(z;g_a)}{G_N}\right)+25.\qquad(4.4)$$

In the case of gravitational wave luminosity distance, the corresponding gravitational wave distance modulus obtained from standard sirens is of the form [110]

$$\mu_{gw}(z;\Omega_m,w,g_a)=5\log_{10}\left(D_L\sqrt{\frac{G_{\rm eff}}{G_N}}\right)+25.\qquad(4.5)$$

In Fig. 12 we show the deviation $\Delta\mu$ as a function of redshift for Ω_m (left panel), w (middle panel), and g_α (right panel) superimposed with JLA SnIa binned data of Table V in the Appendix. The corresponding sensitivity measure is shown in Fig. 13. Notice that even though the deviation $\Delta\mu_{gw}$ appears to be increasing with redshift for all of the parameters considered, the absolute value of the sensitivity measure with respect to the parameter g_a has a maximum for redshifts

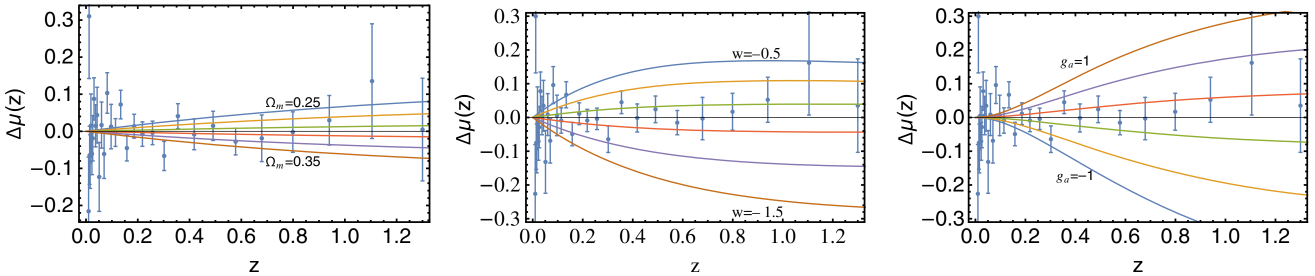

FIG. 12. The deviation of the distance modulus observable $\Delta\mu$ as a function of redshift for Ω_m (left panel), w (middle panel), and g_α (right panel) superimposed with the JLA data of Table V in the Appendix.

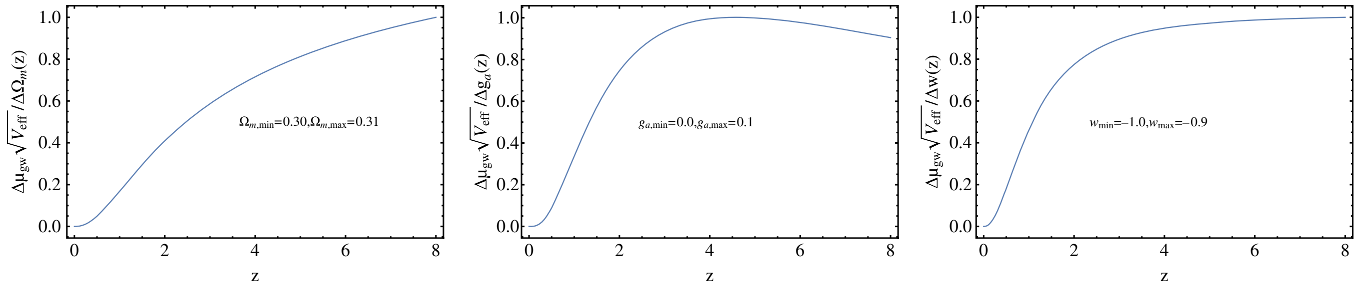

FIG. 13. The sensitivity measure as a function of redshift z for Ω_m (left panel), g_α (middle panel), and w (right panel).

in the range $z \in [4, 5]$, indicating the presence of an optimal redshift range.

The deviations $\Delta\mu_{gw}(z)$ with respect to the parameters Ω_m and w are identical to the corresponding deviations $\Delta\mu(z)$, since for $g_a = 0$ we have $\Delta\mu(z) = \Delta\mu_{gw}(z)$. The deviation $\Delta\mu_{gw}(z)$ with respect to the parameter g_a is shown in Fig. 14 along with the single available data point from the standard siren GW170817 [111,112]. Clearly, even though standard siren data can in principle be used to constrain the evolution of G_{eff}, a dramatic improvement is required before such probes become competitive with growth and SnIa data.

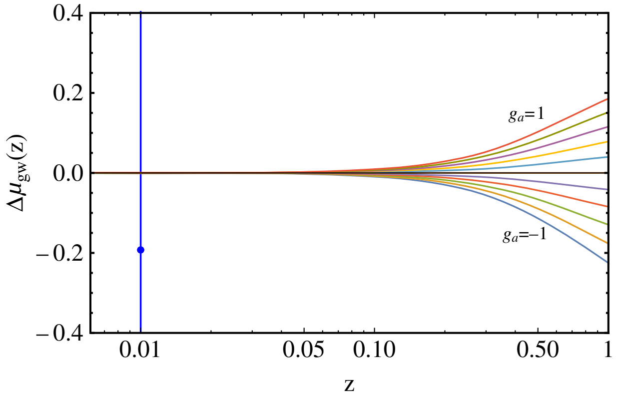

FIG. 14. The deviation of the gravitational wave distance modulus with the parameter g_a. The only existing data point does not lead to any useful constraints.

V. DISCUSSION AND OUTLOOK

We have demonstrated that the constraining power (sensitivity) of a wide range of cosmological observables on cosmological parameters is a rapidly varying function of the redshift where the observable is measured. In fact, this sensitivity in many cases does not vary monotonically with redshift, but rather has degeneracy points (redshift blind spots) and maxima (optimal redshift ranges) which are relatively close in redshift space. The identification of such regions can contribute to the optimal design and redshift-range selection of cosmological probes aimed at constraining specific cosmological parameters through measurements of cosmological observables. In addition, we have shown that many of the recent $f\sigma_8(z)$ RSD data, which tend to be at higher redshifts ($z > 0.8$), are close to blind spots of the observable $f\sigma_8(z)$ with respect to all three cosmological parameters considered (Ω_m, w, and g_a). A similar trend for probing higher redshifts also exists for upcoming surveys, as demonstrated in Table I. A more efficient strategy for this observable would be an improvement of the measurements at lower redshifts instead of focusing on higher redshifts. Such a strategy would lead to improved constraints on all three parameters considered.

Even though our analysis has revealed the generic existence of optimal redshifts and blind spots of observables with respect to specific cosmological parameters, it still has not taken into account all relevant effects that play a role in determining the exact location of these points in redshift space. For example, we have not explicitly taken into account the number of linear modes available to a survey in redshift space as well as the dependence of the effective volume V_{eff} on the number of tracers and their selection. We anticipate that these effects could mildly shift the location of the derived blind spots and optimal redshifts determined by our analysis.

An interesting extension of our analysis could involve the consideration of other observables and additional cosmological parameters (e.g., an equation-of-state parameter that evolves with redshift). The existence of blind spots could be avoided by considering various functions and/or combinations of cosmic observables designed in such a way as to optimize sensitivity for given cosmological parameters in a given redshift range. The investigation of the efficiency of such combinations is also an interesting extension of this project.

ACKNOWLEDGMENTS

We thank the anonymous referee for insightful comments that improved the quality of our paper. This research is cofinanced by Greece and the European Union (European Social Fund- ESF) through the Operational Programme "Human Resources Development, Education and Lifelong Learning" in the context of the project "Strengthening Human Resources Research Potential via Doctorate Research" (MIS-5000432), implemented by the State Scholarships Foundation (IKY). This article has benefited from COST Action CA15117 (CANTATA), supported by COST (European Cooperation in Science and Technology).

APPENDIX: DATA USED IN THE ANALYSIS

In this Appendix we present the data used in the analysis.

TABLE II. The compilation of RSD data used in the present analysis and in the analysis of Ref. [6].

Index	Data set	z	$f\sigma_8(z)$	Refs.	Year	Fiducial cosmology
1	SDSS-LRG	0.35	0.440 ± 0.050	[52]	30 October 2006	$(\Omega_m, \Omega_K, \sigma_8) = (0.25, 0, 0.756)$ [53]
2	VVDS	0.77	0.490 ± 0.18	[52]	6 October 2009	$(\Omega_m, \Omega_K, \sigma_8) = (0.25, 0, 0.78)$
3	2dFGRS	0.17	0.510 ± 0.060	[52]	6 October 2009	$(\Omega_m, \Omega_K) = (0.3, 0, 0.9)$
4	2MRS	0.02	0.314 ± 0.048	[54,55]	13 November 2010	$(\Omega_m, \Omega_K, \sigma_8) = (0.266, 0, 0.65)$
5	SnIa + IRAS	0.02	0.398 ± 0.065	[55,56]	20 October 2011	$(\Omega_m, \Omega_K, \sigma_8) = (0.3, 0, 0.814)$
6	SDSS-LRG-200	0.25	0.3512 ± 0.0583	[57]	9 December 2011	$(\Omega_m, \Omega_K, \sigma_8) = (0.276, 0, 0.8)$
7	SDSS-LRG-200	0.37	0.4602 ± 0.0378	[57]	9 December 2011	
8	SDSS-LRG-60	0.25	0.3665 ± 0.0601	[57]	9 December 2011	$(\Omega_m, \Omega_K, \sigma_8) = (0.276, 0, 0.8)$
9	SDSS-LRG-60	0.37	0.4031 ± 0.0586	[57]	9 December 2011	
10	WiggleZ	0.44	0.413 ± 0.080	[58]	12 June 2012	$(\Omega_m, h, \sigma_8) = (0.27, 0.71, 0.8)$
11	WiggleZ	0.60	0.390 ± 0.063	[58]	12 June 2012	
12	WiggleZ	0.73	0.437 ± 0.072	[58]	12 June 2012	
13	6dFGS	0.067	0.423 ± 0.055	[59]	4 July 2012	$(\Omega_m, \Omega_K, \sigma_8) = (0.27, 0, 0.76)$
14	SDSS-BOSS	0.30	0.407 ± 0.055	[60]	11 August 2012	$(\Omega_m, \Omega_K, \sigma_8) = (0.25, 0, 0.804)$
15	SDSS-BOSS	0.40	0.419 ± 0.041	[60]	11 August 2012	
16	SDSS-BOSS	0.50	0.427 ± 0.043	[60]	11 August 2012	
17	SDSS-BOSS	0.60	0.433 ± 0.067	[60]	11 August 2012	
18	Vipers	0.80	0.470 ± 0.080	[61]	9 July 2013	$(\Omega_m, \Omega_K, \sigma_8) = (0.25, 0, 0.82)$
19	SDSS-DR7-LRG	0.35	0.429 ± 0.089	[62]	8 August 2013	$(\Omega_m, \Omega_K, \sigma_8) = (0.25, 0, 0.809)$ [63]
20	GAMA	0.18	0.360 ± 0.090	[64]	22 September 2013	$(\Omega_m, \Omega_K, \sigma_8) = (0.27, 0, 0.8)$
21	GAMA	0.38	0.440 ± 0.060	[64]	22 September 2013	
22	BOSS-LOWZ	0.32	0.384 ± 0.095	[65]	17 December 2013	$(\Omega_m, \Omega_K, \sigma_8) = (0.274, 0, 0.8)$
23	SDSS DR10 and DR11	0.32	0.48 ± 0.10	[65]	17 December 2013	$(\Omega_m, \Omega_K, \sigma_8) = (0.274, 0, 0.8)$ [66]
24	SDSS DR10 and DR11	0.57	0.417 ± 0.045	[65]	17 December 2013	
25	SDSS-MGS	0.15	0.490 ± 0.145	[67]	30 January 2015	$(\Omega_m, h, \sigma_8) = (0.31, 0.67, 0.83)$
26	SDSS-veloc	0.10	0.370 ± 0.130	[68]	16 June 2015	$(\Omega_m, \Omega_K, \sigma_8) = (0.3, 0, 0.89)$ [69]
27	FastSound	1.40	0.482 ± 0.116	[70]	25 November 2015	$(\Omega_m, \Omega_K, \sigma_8) = (0.27, 0, 0.82)$ [71]
28	SDSS-CMASS	0.59	0.488 ± 0.060	[72]	8 July 2016	$(\Omega_m, h, \sigma_8) = (0.307115, 0.6777, 0.8288)$
29	BOSS DR12	0.38	0.497 ± 0.045	[73]	11 July 2016	$(\Omega_m, \Omega_K, \sigma_8) = (0.31, 0, 0.8)$
30	BOSS DR12	0.51	0.458 ± 0.038	[73]	11 July 2016	
31	BOSS DR12	0.61	0.436 ± 0.034	[73]	11 July 2016	

(Table continued)

TABLE II. *(Continued)*

Index	Data set	z	$f\sigma_8(z)$	Refs.	Year	Fiducial cosmology
32	BOSS DR12	0.38	0.477 ± 0.051	[74]	11 July 2016	$(\Omega_m, h, \sigma_8) = (0.31, 0.676, 0.8)$
33	BOSS DR12	0.51	0.453 ± 0.050	[74]	11 July 2016	
34	BOSS DR12	0.61	0.410 ± 0.044	[74]	11 July 2016	
35	Vipers v7	0.76	0.440 ± 0.040	[75]	26 October 2016	$(\Omega_m, \sigma_8) = (0.308, 0.8149)$
36	Vipers v7	1.05	0.280 ± 0.080	[75]	26 October 2016	
37	BOSS LOWZ	0.32	0.427 ± 0.056	[76]	26 October 2016	$(\Omega_m, \Omega_K, \sigma_8) = (0.31, 0, 0.8475)$
38	BOSS CMASS	0.57	0.426 ± 0.029	[76]	26 October 2016	
39	Vipers	0.727	0.296 ± 0.0765	[77]	21 November 2016	$(\Omega_m, \Omega_K, \sigma_8) = (0.31, 0, 0.7)$
40	6dFGS + SnIa	0.02	0.428 ± 0.0465	[78]	29 November 2016	$(\Omega_m, h, \sigma_8) = (0.3, 0.683, 0.8)$
41	Vipers	0.6	0.48 ± 0.12	[79]	16 December 2016	$(\Omega_m, \Omega_b, n_s, \sigma_8) = (0.3, 0.045, 0.96, 0.831)$ [80]
42	Vipers	0.86	0.48 ± 0.10	[79]	16 December 2016	
43	Vipers PDR-2	0.60	0.550 ± 0.120	[81]	16 December 2016	$(\Omega_m, \Omega_b, \sigma_8) = (0.3, 0.045, 0.823)$
44	Vipers PDR-2	0.86	0.400 ± 0.110	[81]	16 December 2016	
45	SDSS DR13	0.1	0.48 ± 0.16	[82]	22 December 2016	$(\Omega_m, \sigma_8) = (0.25, 0.89)$ [69]
46	2MTF	0.001	0.505 ± 0.085	[83]	16 June 2017	$(\Omega_m, \sigma_8) = (0.3121, 0.815)$
47	Vipers PDR-2	0.85	0.45 ± 0.11	[84]	31 July 2017	$(\Omega_b, \Omega_m, h) = (0.045, 0.30, 0.8)$
48	BOSS DR12	0.31	0.469 ± 0.098	[85]	15 September 2017	$(\Omega_m, h, \sigma_8) = (0.307, 0.6777, 0.8288)$
49	BOSS DR12	0.36	0.474 ± 0.097	[85]	15 September 2017	
50	BOSS DR12	0.40	0.473 ± 0.086	[85]	15 September 2017	
51	BOSS DR12	0.44	0.481 ± 0.076	[85]	15 September 2017	
52	BOSS DR12	0.48	0.482 ± 0.067	[85]	15 September 2017	
53	BOSS DR12	0.52	0.488 ± 0.065	[85]	15 September 2017	
54	BOSS DR12	0.56	0.482 ± 0.067	[85]	15 September 2017	
55	BOSS DR12	0.59	0.481 ± 0.066	[85]	15 September 2017	
56	BOSS DR12	0.64	0.486 ± 0.070	[85]	15 September 2017	
57	SDSS DR7	0.1	0.376 ± 0.038	[86]	12 December 2017	$(\Omega_m, \Omega_b, \sigma_8) = (0.282, 0.046, 0.817)$
58	SDSS-IV	1.52	0.420 ± 0.076	[87]	8 January 2018	$(\Omega_m, \Omega_b h^2, \sigma_8) = (0.26479, 0.02258, 0.8)$
59	SDSS-IV	1.52	0.396 ± 0.079	[88]	8 January 2018	$(\Omega_m, \Omega_b h^2, \sigma_8) = (0.31, 0.022, 0.8225)$
60	SDSS-IV	0.978	0.379 ± 0.176	[89]	9 January 2018	$(\Omega_m, \sigma_8) = (0.31, 0.8)$
61	SDSS-IV	1.23	0.385 ± 0.099	[89]	9 January 2018	
62	SDSS-IV	1.526	0.342 ± 0.070	[89]	9 January 2018	
63	SDSS-IV	1.944	0.364 ± 0.106	[89]	9 January 2018	

TABLE III. A compilation of BAO data that have been published from 2006 until 2018 in chronological order.

Index	z_{eff}	$D_A \times (r_s^{\mathrm{fid}}/r_s)$ (Mpc)	$H(z) \times (r_s/r_s^{\mathrm{fid}})$ (km/ sec Mpc)	$D_V \times (r_s^{\mathrm{fid}}/r_s)$ (Mpc)	Year	Ref.
1	0.275	…	…	1061.87 ± 29	2 November 2009	[113]
2	0.106	…	…	439.3 ± 19.6	16 June 2011	[114]
3	0.35	…	…	1356 ± 25	28 March 2012	[115]
4	0.44	…	…	1716 ± 83	28 July 2014	[105]
5	0.60	…	…	2221 ± 100	28 July 2014	[105]
6	0.73	…	…	2516 ± 86	28 July 2014	[105]
7	0.15	…	…	664 ± 25	21 January 2015	[116]
8	0.38	1100 ± 22	81.5 ± 2.6	1477 ± 16	11 July 2016	[73]
9	0.51	1309.3 ± 24.5	90.5 ± 2.7	1877 ± 19	11 July 2016	[73]
10	0.61	1418 ± 27.3	97.3 ± 2.9	2140 ± 22	11 July 2016	[73]
11	0.32	980.3 ± 15.9	78.4 ± 2.3	1270 ± 14	11 July 2016	[73]
12	0.57	1387.9 ± 22.3	96.6 ± 2.4	2033 ± 21	11 July 2016	[73]
13	0.31	931.42 ± 48	78.3 ± 4.7	1208.36 ± 33.81	6 December 2016	[117]
14	0.36	1047.04 ± 44	77.2 ± 5.7	1388.36 ± 55	6 December 2016	[117]
15	0.40	1131.34 ± 44	79.72 ± 4.9	1560.06 ± 40	6 December 2016	[117]

(Table continued)

TABLE III. *(Continued)*

Index	z_{eff}	$D_A \times (r_s^{\mathrm{fid}}/r_s)$ (Mpc)	$H(z) \times (r_s/r_s^{\mathrm{fid}})$ (km/ sec Mpc)	$D_V \times (r_s^{\mathrm{fid}}/r_s)$ (Mpc)	Year	Ref.
16	0.44	1188.78 ± 32	80.29 ± 3.4	1679.88 ± 35	6 December 2016	[117]
17	0.48	1271.43 ± 25.8	84.69 ± 3.4	1820.44 ± 39	6 December 2016	[117]
18	0.52	1336.53 ± 39	91.97 ± 7.5	1913.54 ± 47	6 December 2016	[117]
19	0.56	1385.47 ± 30.5	97.3 ± 7.9	2001.91 ± 51	6 December 2016	[117]
20	0.59	1423.43 ± 44	97.07 ± 5.8	2100.43 ± 48	6 December 2016	[117]
21	0.64	1448.81 ± 69	97.70 ± 4.8	2207.51 ± 55	6 December 2016	[117]
22	2.33	1669.7 ± 96.1	224 ± 8	…	27 March 2017	[97]
23	1.52	…	…	3843 ± 147	16 October 2017	[118]
24	0.81	1586.7 ± 63.5	…	…	17 December 2017	[119]
25	0.72	…	…	2353 ± 63	21 December 2017	[120]
26	1.52	1850 ± 110	162 ± 12	3985.2 ± 162.4	8 January 2018	[87]
27	0.978	1586.18 ± 284.93	113.72 ± 14.63	2933.59 ± 327.71	16 January 2018	[89]
28	1.230	1769.08 ± 159.67	131.44 ± 12.42	3522.04 ± 192.74	16 January 2018	[89]
29	1.526	1768.77 ± 96.59	148.11 ± 12.75	3954.31 ± 141.71	16 January 2018	[89]
30	1.944	1807.98 ± 146.46	172.63 ± 14.79	4575.17 ± 241.61	16 January 2018	[89]

TABLE IV. The JLA binned data used in the analysis from Ref. [121].

Index	z	μ	σ_μ
1	0.01	32.9539	0.145 886
2	0.012	33.879	0.167 796
3	0.014	33.8421	0.078 498 9
4	0.016	34.1186	0.072 353 9
5	0.019	34.5934	0.085 460 6
6	0.023	34.939	0.056 125 1
7	0.026	35.2521	0.061 068 3
8	0.031	35.7485	0.056 763 9
9	0.037	36.0698	0.056 795 6
10	0.043	36.4346	0.075 143 1
11	0.051	36.6511	0.092 901 3
12	0.06	37.158	0.062 089 2
13	0.07	37.4302	0.065 879 3
14	0.082	37.9566	0.054 650 5
15	0.097	38.2533	0.059 933 7
16	0.114	38.6129	0.037 434 1
17	0.134	39.0679	0.038 614 1
18	0.158	39.3414	0.034 688 6
19	0.186	39.7921	0.032 140 3
20	0.218	40.1565	0.032 961 6
21	0.257	40.565	0.031 719 8
22	0.302	40.9053	0.039 262 2
23	0.355	41.4214	0.033 575 8
24	0.418	41.7909	0.041 520 7
25	0.491	42.2315	0.039 371 3
26	0.578	42.617	0.035 945 3
27	0.679	43.0527	0.062 777 8
28	0.799	43.5042	0.054 591 4
29	0.94	43.9726	0.066 827 6
30	1.105	44.5141	0.154 604
31	1.3	44.8219	0.138 452

TABLE V. The $H(z)$ data compilation presented in Ref. [122] and used in the present analysis.

Index	z	$H(z)$ (km/ sec Mpc)	σ_H	Reference
1	0.070	69	19.6	[123]
2	0.090	69	12	[124]
3	0.120	68.6	26.2	[123]
4	0.170	83	8	[124]
5	0.179	75	4	[125]
6	0.199	75	5	[125]
7	0.200	72.9	29.6	[123]
8	0.240	79.69	6.65	[126]
9	0.270	77	14	[124]
10	0.280	88.8	36.6	[123]
11	0.300	81.7	6.22	[127]
12	0.350	82.7	8.4	[62]
13	0.352	83	14	[125]
14	0.3802	83	13.5	[102]
15	0.400	95	17	[124]
16	0.4004	77	10.02	[102]
17	0.4247	87.1	11.2	[102]
18	0.430	86.45	3.68	[126]
19	0.440	82.6	7.8	[58]
20	0.4497	92.8	12.9	[102]
21	0.4783	80.9	9	[102]
22	0.480	97	62	[128]
23	0.570	92.900	7.855	[129]
24	0.593	104	13	[125]
25	0.6	87.9	6.1	[58]
26	0.68	92	8	[125]
27	0.73	97.3	7.0	[58]
28	0.781	105	12	[125]
29	0.875	125	17	[125]
30	0.88	90	40	[128]
31	0.9	117	23	[124]
32	1.037	154	20	[125]
33	1.300	168	17	[124]
34	1.363	160	22.6	[130]
35	1.43	177	18	[124]
36	1.53	140	14	[124]
37	1.75	202	40	[124]
38	1.965	186.5	50.4	[130]
39	2.300	224	8	[131]
40	2.34	222	7	[132]
41	2.36	226	8	[133]

(Table continued)

TABLE V. (Continued)

---

[1] S. M. Carroll, The cosmological constant, Living Rev. Relativity **4**, 1 (2001).

[2] R. Adam *et al.* (Planck Collaboration), Planck 2015 results. I. Overview of products and scientific results, Astron. Astrophys. **594**, A1 (2016).

[3] N. Aghanim *et al.* (Planck Collaboration), Planck 2018 results. VI. Cosmological parameters, arXiv:1807.06209.

[4] A. G. Riess *et al.*, A 2.4% Determination of the local value of the Hubble constant, Astrophys. J. **826**, 56 (2016).

[5] E. Macaulay, I. Kathrine Wehus, and H. K. Eriksen, Lower Growth Rate from Recent Redshift Space Distortion Measurements than Expected from Planck, Phys. Rev. Lett. **111**, 161301 (2013).

[6] L. Kazantzidis and L. Perivolaropoulos, Evolution of the $f\sigma_8$ tension with the Planck15/ΛCDM determination and implications for modified gravity theories, Phys. Rev. D **97**, 103503 (2018).

[7] S. Nesseris, G. Pantazis, and L. Perivolaropoulos, Tension and constraints on modified gravity parametrizations of $G_{\mathrm{eff}}(z)$ from growth rate and Planck data, Phys. Rev. D **96**, 023542 (2017).

[8] H. Hildebrandt *et al.*, KiDS-450: Cosmological parameter constraints from tomographic weak gravitational lensing, Mon. Not. R. Astron. Soc. **465**, 1454 (2017).

[9] F. Köhlinger *et al.*, KiDS-450: The tomographic weak lensing power spectrum and constraints on cosmological parameters, Mon. Not. R. Astron. Soc. **471**, 4412 (2017).

[10] G. Hinshaw *et al.* (WMAP Collaboration), Nine-year Wilkinson microwave anisotropy probe (WMAP) observations: Cosmological parameter results, Astrophys. J. Suppl. Ser. **208**, 19 (2013).

[11] S. Naess *et al.* (ACTPol Collaboration), The Atacama cosmology telescope: CMB polarization at $200 < \ell < 9000$, J. Cosmol. Astropart. Phys. 10 (2014) 007.

[12] R. Keisler *et al.* (SPT Collaboration), Measurements of sub-degree B-mode polarization in the cosmic microwave background from 100 square degrees of SPTpol data, Astrophys. J. **807**, 151 (2015).

[13] S. W. Henderson *et al.*, Advanced ACTPol cryogenic detector arrays and readout, J. Low Temp. Phys. **184**, 772 (2016).

[14] R. Keisler *et al.* (SPT Collaboration), Measurements of sub-degree B-mode polarization in the cosmic microwave background from 100 square degrees of SPTpol data, Astrophys. J. **807**, 151 (2015).

[15] K. N. Abazajian *et al.* (CMB-S4 Collaboration), *CMB-S4 Science Book*, 1st ed. (2016).

[16] A. Suzuki *et al.*, The LiteBIRD Satellite Mission—Sub-Kelvin Instrument, J. Low Temp. Phys. **193**, 1048 (2018).

[17] T. Matsumura *et al.*, Mission design of LiteBIRD, J. Low Temp. Phys. **176**, 733 (2014).

[18] C. Heymans *et al.*, CFHTLenS: The Canada-France-Hawaii telescope lensing survey, Mon. Not. R. Astron. Soc. **427**, 146 (2012).

[19] K. S. Dawson *et al.*, The SDSS-IV extended Baryon Oscillation Spectroscopic Survey: Overview and early data, Astron. J. **151**, 44 (2016).

[20] T. Abbott *et al.* (DES Collaboration), Cosmology from cosmic shear with dark energy survey science verification data, Phys. Rev. D **94**, 022001 (2016).

[21] M. A. Troxel *et al.* (DES Collaboration), Dark energy survey year 1 results: Cosmological constraints from cosmic shear, Phys. Rev. D **98**, 043528 (2018).

[22] T. M. C. Abbott *et al.* (DES Collaboration), Dark energy survey year 1 results: Cosmological constraints from galaxy clustering and weak lensing, Phys. Rev. D **98**, 043526 (2018).

[23] Y.-K. Chiang *et al.*, Surveying galaxy proto-clusters in emission: A large-scale structure at $z = 2.44$ and the outlook for HETDEX, Astrophys. J. **808**, 37 (2015).

[24] P. A. Abell *et al.* (LSST Science and LSST Project), *LSST Science Book, Version 2.0* (2009).

[25] P. Marshall *et al.* (LSST Collaboration), Science-driven optimization of the LSST observing strategy, arXiv:1708.04058.

[26] P. Bull, P. G. Ferreira, P. Patel, and M. G. Santos, Late-time cosmology with 21 cm intensity mapping experiments, Astrophys. J. **803**, 21 (2015).

[27] M. J. Jarvis, D. Bacon, C. Blake, M. L. Brown, S. N. Lindsay, A. Raccanelli, M. Santos, and D. Schwarz, Cosmology with SKA radio continuum surveys, arXiv:1501.03825.

[28] D. Bacon *et al.*, Synergy between the large synoptic survey telescope and the square kilometre array, Proc. Sci. AASKA14 (**2015**) 145.

[29] S. Yahya, P. Bull, M. G. Santos, M. Silva, R. Maartens, P. Okouma, and B. Bassett, Cosmological performance of SKA HI galaxy surveys, Mon. Not. R. Astron. Soc. **450**, 2251 (2015).

[30] R. Laureijs *et al.* (EUCLID Collaboration), Euclid definition study report, arXiv:1110.3193.

[31] L. Amendola *et al.*, Cosmology and fundamental physics with the Euclid satellite, Living Rev. Relativity **21**, 2 (2018).

[32] D. Spergel *et al.*, Wide-Field infrarRed survey telescope-astrophysics focused telescope assets WFIRST-AFTA 2015 report, arXiv:1503.03757.

[33] R. Hounsell *et al.*, Simulations of the WFIRST supernova survey and forecasts of cosmological constraints, Astrophys. J. **867**, 23 (2018).

[34] S. Nesseris, C. Blake, T. Davis, and D. Parkinson, The WiggleZ dark energy survey: Constraining the evolution of Newton's constant using the growth rate of structure, J. Cosmol. Astropart. Phys. 07 (2011) 037.

[35] L. Anderson *et al.* (BOSS Collaboration), The clustering of galaxies in the SDSS-III Baryon Oscillation Spectroscopic Survey: Baryon acoustic oscillations in the data releases 10 and 11 galaxy samples, Mon. Not. R. Astron. Soc. **441**, 24 (2014).

[36] L. Samushia *et al.*, The clustering of galaxies in the SDSS-III Baryon Oscillation Spectroscopic Survey: Measuring growth rate and geometry with anisotropic clustering, Mon. Not. R. Astron. Soc. **439**, 3504 (2014).

[37] A. Aghamousa *et al.* (DESI Collaboration), The DESI experiment Part I: Science, targeting, and survey design, arXiv:1611.00036.

[38] A. Aghamousa *et al.* (DESI Collaboration), The DESI experiment Part II: Instrument design, arXiv:1611.00037.

[39] https://www.desi.lbl.gov/.

[40] http://sci.esa.int/euclid/.

[41] S. Nesseris and Leandros Perivolaropoulos, The limits of extended quintessence, Phys. Rev. D **75**, 023517 (2007).

[42] C. J. Copi, A. N. Davis, and L. M. Krauss, A New nucleosynthesis constraint on the variation of G, Phys. Rev. Lett. **92**, 171301 (2004).

[43] W. J. Percival, Cosmological structure formation in a homogeneous dark energy background, Astron. Astrophys. **443**, 819 (2005).

[44] A. Gomez-Valent and J. Sola, Relaxing the σ_8-tension through running vacuum in the Universe, Europhys. Lett. **120**, 39001 (2017).

[45] A. Gómez-Valent and J. Solà, Density perturbations for running vacuum: A successful approach to structure formation and to the σ_8-tension, Mon. Not. R. Astron. Soc. **478**, 126 (2018).

[46] S. Basilakos and S. Nesseris, Conjoined constraints on modified gravity from the expansion history and cosmic growth, Phys. Rev. D **96**, 063517 (2017).

[47] S. Basilakos and S. Nesseris, Testing Einstein's gravity and dark energy with growth of matter perturbations: Indications for new physics, Phys. Rev. D **94**, 123525 (2016).

[48] S. Alam, S. Ho, and A. Silvestri, Testing deviations from ΛCDM with growth rate measurements from six large-scale structure surveys at $z = 0.06$–1, Mon. Not. R. Astron. Soc. **456**, 3743 (2016).

[49] B. L'Huillier, A. Shafieloo, and H. Kim, Model-independent cosmological constraints from growth and expansion, Mon. Not. R. Astron. Soc. **476**, 3263 (2018).

[50] B. Sagredo, S. Nesseris, and D. Sapone, Internal robustness of growth rate data, Phys. Rev. D **98**, 083543 (2018).

[51] R. Arjona, W. Cardona, and S. Nesseris, Unraveling the effective fluid approach for $f(R)$ models in the subhorizon approximation, Phys. Rev. D **99**, 043516 (2019).

[52] Y.-S. Song and W. J. Percival, Reconstructing the history of structure formation using Redshift Distortions, J. Cosmol. Astropart. Phys. 10 (2009) 004.

[53] M. Tegmark *et al.* (SDSS Collaboration), Cosmological constraints from the SDSS luminous red galaxies, Phys. Rev. D **74**, 123507 (2006).

[54] M. Davis, A. Nusser, K. Masters, C. Springob, J. P. Huchra, and G. Lemson, Local gravity versus local velocity: Solutions for β and nonlinear bias, Mon. Not. R. Astron. Soc. **413**, 2906 (2011).

[55] M. J. Hudson and S. J. Turnbull, The growth rate of cosmic structure from peculiar velocities at low and high redshifts, Astrophys. J. Lett. **751**, L30 (2012).

[56] S. J. Turnbull, M. J. Hudson, H. A. Feldman, M. Hicken, R. P. Kirshner, and R. Watkins, Cosmic flows in the nearby universe from type ia supernovae, Mon. Not. R. Astron. Soc. **420**, 447 (2012).

[57] L. Samushia, W. J. Percival, and A. Raccanelli, Interpreting large-scale redshift-space distortion measurements, Mon. Not. R. Astron. Soc. **420**, 2102 (2012).

[58] C. Blake *et al.*, The WiggleZ dark energy survey: Joint measurements of the expansion and growth history at z1, Mon. Not. R. Astron. Soc. **425**, 405 (2012).

[59] F. Beutler, C. Blake, M. Colless, D. H. Jones, L. Staveley-Smith, G. B. Poole, L. Campbell, Q. Parker, W. Saunders, and F. Watson, The 6df galaxy survey: $z \approx 0$ measurements of the growth rate and $\sigma 8$, Mon. Not. R. Astron. Soc. **423**, 3430 (2012).

[60] R. Tojeiro *et al.*, The clustering of galaxies in the sdss-iii Baryon Oscillation Spectroscopic Survey: Measuring structure growth using passive galaxies, Mon. Not. R. Astron. Soc. **424**, 2339 (2012).

[61] S. de la Torre *et al.*, The VIMOS Public Extragalactic Redshift Survey (VIPERS). Galaxy clustering and redshift-space distortions at $z = 0.8$ in the first data release, Astron. Astrophys. **557**, A54 (2013).

[62] C.-H. Chuang and Y. Wang, Modelling the anisotropic two-point galaxy correlation function on small scales and single-probe measurements of $h(z)$, $da(z)$ and $f(z)\sigma 8(z)$ from the Sloan Digital Sky Survey dr7 luminous red galaxies, Mon. Not. R. Astron. Soc. **435**, 255 (2013).

[63] E. Komatsu *et al.* (WMAP Collaboration), Seven-year Wilkinson microwave anisotropy probe (WMAP) observations: Cosmological interpretation, Astrophys. J. Suppl. Ser. **192**, 18 (2011).

[64] C. Blake *et al.*, Galaxy and mass assembly (GAMA): Improved cosmic growth measurements using multiple tracers of large-scale structure, Mon. Not. R. Astron. Soc. **436**, 3089 (2013).

[65] A. G. Sanchez *et al.*, The clustering of galaxies in the SDSS-III Baryon Oscillation Spectroscopic Survey: Cosmological implications of the full shape of the clustering wedges in the data release 10 and 11 galaxy samples, Mon. Not. R. Astron. Soc. **440**, 2692 (2014).

[66] L. Anderson *et al.* (BOSS Collaboration), The clustering of galaxies in the SDSS-III Baryon Oscillation Spectroscopic Survey: Baryon acoustic oscillations in the data releases 10 and 11 galaxy samples, Mon. Not. R. Astron. Soc. **441**, 24 (2014).

[67] C. Howlett, A. Ross, L. Samushia, W. Percival, and M. Manera, The clustering of the SDSS main galaxy sample—II. Mock galaxy catalogues and a measurement of the growth of structure from redshift space distortions at $z = 0.15$, Mon. Not. R. Astron. Soc. **449**, 848 (2015).

[68] M. Feix, A. Nusser, and E. Branchini, Growth Rate of Cosmological Perturbations at $z \approx 0.1$ from a New Observational Test, Phys. Rev. Lett. **115**, 011301 (2015).

[69] M. Tegmark *et al.* (SDSS Collaboration), The 3-D power spectrum of galaxies from the SDSS, Astrophys. J. **606**, 702 (2004).

[70] T. Okumura *et al.*, The subaru FMOS galaxy redshift survey (FastSound). IV. New constraint on gravity theory from redshift space distortions at $z \sim 1.4$, Publ. Astron. Soc. Jpn. **68**, 38 (2016).

[71] G. Hinshaw *et al.* (WMAP Collaboration), Nine-year Wilkinson microwave anisotropy probe (WMAP) observations: Cosmological parameter results, Astrophys. J. Suppl. Ser. **208**, 19 (2013).

[72] C.-H. Chuang *et al.*, The clustering of galaxies in the SDSS-III Baryon Oscillation Spectroscopic Survey: Single-probe measurements from CMASS anisotropic galaxy clustering, Mon. Not. R. Astron. Soc. **461**, 3781 (2016).

[73] S. Alam *et al.* (BOSS Collaboration), The clustering of galaxies in the completed SDSS-III Baryon Oscillation Spectroscopic Survey: Cosmological analysis of the DR12 galaxy sample, Mon. Not. R. Astron. Soc. **470**, 2617 (2017).

[74] F. Beutler *et al.* (BOSS Collaboration), The clustering of galaxies in the completed SDSS-III Baryon Oscillation Spectroscopic Survey: Anisotropic galaxy clustering in Fourier-space, Mon. Not. R. Astron. Soc. **466**, 2242 (2017).

[75] M. J. Wilson, Geometric and growth rate tests of General Relativity with recovered linear cosmological perturbations, Ph.D. thesis, Edinburgh University, 2016.

[76] H. Gil-Marín, W. J. Percival, L. Verde, J. R. Brownstein, C.-H. Chuang, F.-S. Kitaura, S. A. Rodríguez-Torres, and M. D. Olmstead, The clustering of galaxies in the SDSS-III Baryon Oscillation Spectroscopic Survey: RSD measurement from the power spectrum and bispectrum of the DR12 BOSS galaxies, Mon. Not. R. Astron. Soc. **465**, 1757 (2017).

[77] A. J. Hawken *et al.*, The VIMOS Public Extragalactic Redshift Survey: Measuring the growth rate of structure around cosmic voids, Astron. Astrophys. **607**, A54 (2017).

[78] D. Huterer, D. Shafer, D. Scolnic, and F. Schmidt, Testing ΛCDM at the lowest redshifts with SN Ia and galaxy velocities, J. Cosmol. Astropart. Phys. 05 (2017) 015.

[79] S. de la Torre *et al.*, The VIMOS Public Extragalactic Redshift Survey (VIPERS). Gravity test from the combination of redshift-space distortions and galaxy-galaxy lensing at $0.5 < z < 1.2$, Astron. Astrophys. **608**, A44 (2017).

[80] P. A. R. Ade *et al.* (Planck Collaboration), Planck 2015 results. XIII. Cosmological parameters, Astron. Astrophys. **594**, A13 (2016).

[81] A. Pezzotta *et al.*, The VIMOS Public Extragalactic Redshift Survey (VIPERS): The growth of structure at $0.5 < z < 1.2$ from redshift-space distortions in the clustering of the PDR-2 final sample, Astron. Astrophys. **604**, A33 (2017).

[82] M. Feix, E. Branchini, and A. Nusser, Speed from light: Growth rate and bulk flow at $z \approx 0.1$ from improved SDSS DR13 photometry, Mon. Not. R. Astron. Soc. **468**, 1420 (2017).

[83] C. Howlett, L. Staveley-Smith, P. J. Elahi, T. Hong, T. H. Jarrett, D. H. Jones, B. S. Koribalski, L. M. Macri, K. L. Masters, and C. M. Springob, 2MTF VI. Measuring the velocity power spectrum, Mon. Not. R. Astron. Soc. **471**, 3135 (2017).

[84] F. G. Mohammad *et al.*, The VIMOS Public Extragalactic Redshift Survey (VIPERS): An unbiased estimate of the growth rate of structure at $\langle \mathbf{z} \rangle = \mathbf{0.85}$ using the clustering of luminous blue galaxies, Astron. Astrophys. **610**, A59 (2018).

[85] Y. Wang, G.-B. Zhao, C.-H. Chuang, M. Pellejero-Ibanez, C. Zhao, F.-S. Kitaura, and S. Rodriguez-Torres, The clustering of galaxies in the completed SDSS-III Baryon

Oscillation Spectroscopic Survey: A tomographic analysis of structure growth and expansion rate from anisotropic galaxy clustering, Mon. Not. Roy. Astron. Soc. **481**, 3160 (2018).

[86] F. Shi *et al.*, Mapping the real space distributions of galaxies in SDSS DR7: II. Measuring the growth rate, linear mass variance and biases of galaxies at redshift 0.1, Astrophys. J. **861**, 137 (2018).

[87] H. Gil-Marín *et al.*, The clustering of the SDSS-IV extended Baryon Oscillation Spectroscopic Survey DR14 quasar sample: Structure growth rate measurement from the anisotropic quasar power spectrum in the redshift range $0.8 < z < 2.2$, Mon. Not. R. Astron. Soc. **477**, 1604 (2018).

[88] J. Hou *et al.*, The clustering of the SDSS-IV extended Baryon Oscillation Spectroscopic Survey DR14 quasar sample: Anisotropic clustering analysis in configuration-space, Mon. Not. R. Astron. Soc. **480**, 2521 (2018).

[89] G.-B. Zhao *et al.*, The clustering of the SDSS-IV extended Baryon Oscillation Spectroscopic Survey DR14 quasar sample: A tomographic measurement of cosmic structure growth and expansion rate based on optimal redshift weights, Mon. Not. R. Astron. Soc., **482**, 3497 (2019).

[90] H. A. Feldman, N. Kaiser, and J. A. Peacock, Power spectrum analysis of three-dimensional redshift surveys, Astrophys. J. **426**, 23 (1994).

[91] S. F Huelga, C. Macchiavello, T. Pellizzari, A. K. Ekert, M. B. Plenio, and J. I. Cirac, On the improvement of frequency standards with quantum entanglement, Phys. Rev. Lett. **79**, 3865 (1997).

[92] A. R. Duffy, Probing the nature of dark energy through galaxy redshift surveys with radio telescopes, Ann. Phys. (Amsterdam) **526**, 283 (2014).

[93] F. B. Abdalla and S. Rawlings, Probing dark energy with baryonic oscillations and future radio surveys of neutral hydrogen, Mon. Not. R. Astron. Soc. **360**, 27 (2005).

[94] R. Gannouji, L. Kazantzidis, L. Perivolaropoulos, and D. Polarski, Consistency of modified gravity with a decreasing $G_{\mathrm{eff}}(z)$ in a ΛCDM background, Phys. Rev. D **98**, 104044 (2018).

[95] E. Komatsu *et al.* (WMAP Collaboration), Five-year Wilkinson microwave anisotropy probe (WMAP) observations: Cosmological interpretation, Astrophys. J. Suppl. Ser. **180**, 330 (2009).

[96] É. Aubourg *et al.*, Cosmological implications of baryon acoustic oscillation measurements, Phys. Rev. D **92**, 123516 (2015).

[97] J. E. Bautista *et al.*, Measurement of baryon acoustic oscillation correlations at $z = 2.3$ with SDSS DR12 Lyα-forests, Astron. Astrophys. **603**, A12 (2017).

[98] C. Alcock and B. Paczynski, An evolution free test for non-zero cosmological constant, Nature (London) **281**, 358 (1979).

[99] A. Lewis, A. Challinor, and A. Lasenby, efficient computation of CMB anisotropies in closed FRW models, Astrophys. J. **538**, 473 (2000).

[100] D. J. Eisenstein and W. Hu, Baryonic features in the matter transfer function, Astrophys. J. **496**, 605 (1998).

[101] J. Hamann, S. Hannestad, J. Lesgourgues, C. Rampf, and Y. Y. Y. Wong, Cosmological parameters from large scale structure—geometric versus shape information, J. Cosmol. Astropart. Phys. 07 (2010) 022.

[102] M. Moresco, L. Pozzetti, A. Cimatti, R. Jimenez, C. Maraston, L. Verde, D. Thomas, A. Citro, R. Tojeiro, and D. Wilkinson, A 6% measurement of the Hubble parameter at $z \sim 0.45$: Direct evidence of the epoch of cosmic re-acceleration, J. Cosmol. Astropart. Phys. 05 (2016) 014.

[103] F. K. Anagnostopoulos and S. Basilakos, Constraining the dark energy models with $H(z)$ data: An approach independent of H_0, Phys. Rev. D **97**, 063503 (2018).

[104] R.-Y. Guo and X. Zhang, Constraining dark energy with Hubble parameter measurements: An analysis including future redshift-drift observations, Eur. Phys. J. C **76**, 163 (2016).

[105] E. A. Kazin *et al.*, The WiggleZ dark energy survey: Improved distance measurements to $z = 1$ with reconstruction of the baryonic acoustic feature, Mon. Not. R. Astron. Soc. **441**, 3524 (2014).

[106] See Supplemental Material at http://link.aps.org/supplemental/10.1103/PhysRevD.99.063537 for details about the MATHEMATICA files used for the numerical analysis and the construction of the figures. This material is also available at http://leandros.physics.uoi.gr/opt-redshift/.

[107] E. Garcia-Berro, E. Gaztanaga, J. Isern, O. Benvenuto, and L. Althaus, On the evolution of cosmological type ia supernovae and the gravitational constant, arXiv:astro-ph/9907440.

[108] E. Gaztanaga, E. Garcia-Berro, J. Isern, E. Bravo, and I. Dominguez, Bounds on the possible evolution of the gravitational constant from cosmological type Ia supernovae, Phys. Rev. D **65**, 023506 (2001).

[109] S. Nesseris and L. Perivolaropoulos, Evolving newton's constant, extended gravity theories and SnIa data analysis, Phys. Rev. D **73**, 103511 (2006).

[110] E. Belgacem, Y. Dirian, S. Foffa, and M. Maggiore, Gravitational-wave luminosity distance in modified gravity theories, Phys. Rev. D **97**, 104066 (2018).

[111] B. P. Abbott *et al.* (LIGO Scientific and Virgo Collaborations), Gw170817: Observation of Gravitational Waves from a Binary Neutron Star Inspiral, Phys. Rev. Lett. **119**, 161101 (2017).

[112] B. P. Abbott *et al.* (LIGO Scientific, VINROUGE, Las Cumbres Observatory, DES, DLT40, Virgo, 1M2H, Dark Energy Camera GW-E, and MASTER Collaborations), A gravitational-wave standard siren measurement of the Hubble constant, Nature (London) **551**, 85 (2017).

[113] W. J. Percival *et al.* (SDSS Collaboration), Baryon acoustic oscillations in the Sloan Digital Sky Survey data release 7 galaxy sample, Mon. Not. R. Astron. Soc. **401**, 2148 (2010).

[114] F. Beutler, C. Blake, M. Colless, D. H. Jones, L. Staveley-Smith, L. Campbell, Q. Parker, W. Saunders, and F. Watson, The 6dF galaxy survey: Baryon acoustic oscillations and the local Hubble constant, Mon. Not. R. Astron. Soc. **416**, 3017 (2011).

[115] K. T. Mehta, A. J. Cuesta, X. Xu, D. J. Eisenstein, and N. Padmanabhan, A 2% distance to $z = 0.35$ by reconstructing baryon acoustic oscillations—III: Cosmological measurements and interpretation, Mon. Not. Roy. Astron. Soc. **427**, 2168 (2012).

[116] A. J. Ross, L. Samushia, C. Howlett, W. J. Percival, A. Burden, and M. Manera, The clustering of the SDSS DR7 main galaxy sample—I. A 4 per cent distance measure at $z = 0.15$, Mon. Not. R. Astron. Soc. **449**, 835 (2015).

[117] G.-B. Zhao *et al.* (BOSS Collaboration), The clustering of galaxies in the completed SDSS-III Baryon Oscillation Spectroscopic Survey: Tomographic BAO analysis of DR12 combined sample in Fourier space, Mon. Not. R. Astron. Soc. **466**, 762 (2017).

[118] M. Ata *et al.*, The clustering of the SDSS-IV extended Baryon Oscillation Spectroscopic Survey DR14 quasar sample: First measurement of baryon acoustic oscillations between redshift 0.8 and 2.2, Mon. Not. R. Astron. Soc. **473**, 4773 (2018).

[119] T. M. C. Abbott *et al.* (DES Collaboration), Dark energy survey year 1 results: Measurement of the baryon acoustic oscillation scale in the distribution of galaxies to redshift 1, arXiv:1712.06209.

[120] J. E. Bautista *et al.*, The SDSS-IV extended Baryon Oscillation Spectroscopic Survey: Baryon acoustic oscillations at redshift of 0.72 with the DR14 luminous red galaxy sample, arXiv:1712.08064.

[121] M. Betoule *et al.* (SDSS Collaboration), Improved cosmological constraints from a joint analysis of the SDSS-II and SNLS supernova samples, Astron. Astrophys. **568**, A22 (2014).

[122] J. F. Jesus, T. M. Gregório, F. Andrade-Oliveira, R. Valentim, and C. A. O. Matos, Bayesian correction of $H(z)$ data uncertainties, Mon. Not. R. Astron. Soc. **477**, 2867 (2018).

[123] C. Zhang, H. Zhang, S. Yuan, T.-J. Zhang, and Y.-C. Sun, Four new observational $H(z)$ data from luminous red galaxies in the Sloan Digital Sky Survey data release seven, Res. Astron. Astrophys. **14**, 1221 (2014).

[124] J. Simon, L. Verde, and R. Jimenez, Constraints on the redshift dependence of the dark energy potential, Phys. Rev. D **71**, 123001 (2005).

[125] M. Moresco *et al.*, Improved constraints on the expansion rate of the Universe up to z 1.1 from the spectroscopic evolution of cosmic chronometers, J. Cosmol. Astropart. Phys. 08 (2012) 006.

[126] E. Gaztanaga, A. Cabre, and L. Hui, Clustering of luminous red galaxies IV: Baryon acoustic peak in the line-of-sight direction and a direct measurement of H(z), Mon. Not. R. Astron. Soc. **399**, 1663 (2009).

[127] A. Oka, S. Saito, T. Nishimichi, A. Taruya, and K. Yamamoto, Simultaneous constraints on the growth of structure and cosmic expansion from the multipole power spectra of the SDSS DR7 LRG sample, Mon. Not. R. Astron. Soc. **439**, 2515 (2014).

[128] D. Stern, R. Jimenez, L. Verde, M. Kamionkowski, and S. A. Stanford, Cosmic chronometers: Constraining the equation of state of dark energy. I: H(z) measurements, J. Cosmol. Astropart. Phys. 02 (2010) 008.

[129] L. Anderson *et al.*, The clustering of galaxies in the SDSS-III Baryon Oscillation Spectroscopic Survey: Measuring D_A and H at $z = 0.57$ from the baryon acoustic peak in the data release 9 spectroscopic galaxy sample, Mon. Not. R. Astron. Soc. **439**, 83 (2014).

[130] M. Moresco, Raising the bar: New constraints on the Hubble parameter with cosmic chronometers at z 2, Mon. Not. R. Astron. Soc. **450**, L16 (2015).

[131] N. G. Busca *et al.*, Baryon acoustic oscillations in the Ly-α forest of BOSS quasars, Astron. Astrophys. **552**, A96 (2013).

[132] T. Delubac *et al.* (BOSS Collaboration), Baryon acoustic oscillations in the Lya forest of BOSS DR11 quasars, Astron. Astrophys. **574**, A59 (2015).

[133] A. Font-Ribera *et al.* (BOSS Collaboration), Quasar-Lyman α forest cross-correlation from BOSS DR11: Baryon acoustic oscillations, J. Cosmol. Astropart. Phys. 05 (2014) 027.